

MULTIMODAL EVALUATION OF THE LITHIUM ION BATTERY SOLID
ELECTROLYTE INTERPHASE: QUANTIFYING ELEMENTARY CHEMISTRY VIA *IN*
OPERANDO NEUTRON REFLECTIVITY AND ELECTROCHEMICAL QUARTZ
CRYSTAL MICROBALANCE

by

Christopher H. Lee

A thesis submitted to the Faculty and the Board of Trustees of the Colorado School of Mines in partial fulfillment of the requirements for the degree of Master of Science (Mechanical Engineering).

Golden, Colorado

Date _____

Signed: _____
Christopher H. Lee

Signed: _____
Dr. Steven DeCaluwe
Thesis Advisor

Golden, Colorado

Date _____

Signed: _____
Dr. Gregory Jackson
Professor and Head
Department of Mechanical Engineering

ABSTRACT

The solid electrolyte interphase (SEI) is an interfacial layer that forms in lithium-ion batteries due to instability of the electrolyte at low voltages. While the SEI in theory passivates the electrolyte from further degradation, in reality continued SEI growth shortens battery lifetime and leads to myriad problems, including capacity fade, reduced charge/discharge rates, and contributions to thermal runaway and catastrophic battery fires. Despite years of study, the SEI remains a central challenge to lithium-ion battery durability, largely due to poor understanding of the basic chemistry responsible for its formation and evolution.

Neutron reflectometry (NR) is a promising technique that is able to characterize the SEI layer under a range of electrochemical and thermal conditions. Neutrons can penetrate many sample environments with little attenuation, are sensitive to isotopes of elements such as Li and H, and impart little ionizing or thermal energy. Furthermore, NR provides sub-Ångström sensitivity for the layer thickness, making NR perhaps the perfect *in operando* probe for enhancing the understanding of SEI chemistry. Although initial NR studies of the SEI show great sensitivity to the chemistry and thickness of the SEI, additional sensitivity is required to provide true quantitative insight into phenomena such as the layered ordering of the SEI, its evolution as a function of electric potential, and its thermal degradation at elevated temperatures.

This study extends neutron reflectometry experiments published in 2012 on the SEI by improving the ability of the technique to quantify the chemistry and structure of the SEI. These improvements include fabrication and optimization of non-intercalating anodes for enhanced NR contrast and the use of complementary electrochemical measurements and mass uptake measurements via quartz crystal microbalance with dissipation (QCM-D). In this study, an SEI is

grown on a non-intercalating, thin-film W anode via CV, and its properties are measured *in operando* by parallel NR and QCM-D measurements to create a depth profile of the SEI chemical composition. A dual-layer SEI structure is observed, which has been proposed in literature based on other techniques but has never previously been observed *in operando* via NR. The NR data and QCM-D data are then combined to create a proposed chemical composition as well as physical structure, which shows an inner layer (adjacent to the electrode) that is composed mainly of Li₂O (25%), LiF (20%), LiOH (27%), Li₂CO₃ (15.5%), and electrolyte (12.5%), and an outer layer (adjacent to the electrolyte) of LEDC (51%), LEC (6%), and electrolyte (43%). This study not only opens the way for highly sensitive NR measurements, it allows for a detailed *quantitative* understanding of the SEI composition and formation chemistry, which has previously not been well explored.

TABLE OF CONTENTS

ABSTRACT.....	iii
LIST OF FIGURES	viii
LIST OF TABLES	x
ACKNOWLEDGEMENTS	xi
CHAPTER 1 INTRODUCTION	1
1.1 Background.....	3
1.1.1 Device Operation and Material Choices	3
1.1.2 The Solid Electrolyte Interphase	5
1.2 Project Objectives	8
CHAPTER 2 EXPERIMENTAL TECHNIQUES.....	11
2.1 Neutron Reflectometry.....	11
2.1.1 Principles of Operation.....	11
2.1.2 Advantages of Neutron Reflectometry.....	14
2.1.3 Challenges of Neutron Reflectometry.....	15
2.1.4 Fitting NR Data	16
2.2 Electrochemical Quartz Crystal Microbalance with Dissipation Monitoring.....	18
2.2.1 Quartz Crystal Microbalance with Dissipation Monitoring.....	18
2.2.2 Electrochemical Measurements.....	20
2.3 Conclusion	22
CHAPTER 3 THIN FILM ANODE FABRICATION	23
3.1 Electrode Material Choice	24

3.2	Optimization of Tungsten Deposition.....	26
3.3	Conclusion	33
CHAPTER 4 EXPERIMENTAL RESULTS		34
4.1	Materials and Methods.....	34
4.1.1	EQCM-D Equipment.....	34
4.1.2	EQCM-D Experimental Procedure	35
4.1.3	Neutron Facilities	36
4.1.4	NR Measurement of As-Grown Electrode	36
4.1.5	NR Measurement of the Battery Cell at OCV.....	36
4.1.6	NR Measurement of the Non-Electrochemical Wet Cell.....	40
4.1.7	NR Data Fitting	40
4.2	Results.....	42
4.3	EQCM-D Experimental Results	42
4.3.1	NR Experimental Results	46
4.3.1.1	Substrate Layer (Si, SiO ₂ , and W) Parameters.....	46
4.3.1.2	Analysis of the Electrode-Electrolyte Interface – Identification of the SEI	50
4.4	Conclusion	53
CHAPTER 5 SEI FORMATION AND COMPOSITION ANALYSIS.....		54
5.1	Mass Per Electron (m.p.e.) Analysis.....	54
5.2	Composition Analysis by Monte Carlo Simulation	56
5.3	Conclusion	63
CHAPTER 6 FUTURE WORK AND CONCLUSION		65
6.1	Future Work	65

6.1.1	Improved NR Cell Design and High-Temperature Measurements	65
6.1.2	SEI Characterization for Varying Electrolyte Composition	66
6.1.3	Refinement of the Monte Carlo Simulator	67
6.1.4	Structural Study of the Thermal Oxide on the Working Electrode	67
6.1.5	NR Comparison of the Shorted Cell vs. a Cycled Cell	67
6.2	Conclusion	68
REFERENCES CITED		71
APPENDIX A – NR FITTING PYTHON SCRIPTS		77
A.1	W1_bare and W1_ocv Simultaneous Fitting Script	77
A.2	W2_electrolyte Fitting Script	80

LIST OF FIGURES

Figure 1.1: Lithium-ion battery operation. <i>Adopted from Teki, R. et al. Nanostructured Silicon Anodes for Lithium Rechargeable Batteries</i> , 2009 [16].	4
Figure 1.2: Schematic showing the electrochemical stability window for an electrolyte. Φ_A and Φ_C are the work functions for the anode and cathode. Adopted from J. B. Goodenough and Y. Kim, <i>Challenges for Rechargeable Li Batteries</i> , 2010.	6
Figure 2.1: Graphic demonstrating how path length differences cause phase shifts in reflected neutrons. Courtesy of Dr. Joseph Dura, NIST.	12
Figure 2.2: Graphic showing the inverse relation between layer thickness and Kiessig fringe period. The raw reflectivity data can be fitted to obtain a more intuitive fitted SLD profile. Courtesy of Dr. Joseph Dura, NIST.	12
Figure 2.3: Demonstration of the effect of both rigid and elastic layers on the effect of QCM-D data. Adopted from Biolin Scientific, <i>Quartz Crystal Microbalance</i> , 2016 [55].	20
Figure 3.1: Simulated NR reflectivity plots comparing various anode materials with and without an SEI layer. (a) Copper anode; (b) Gold anode; (c) Tungsten anode; (d) Titanium Nitride anode	24
Figure 3.2: 3D plots of AFM scans for a tungsten thin film under different deposition conditions. (a) 50 W, 10 mTorr; (b) 15 W, 3 mTorr	27
Figure 3.3: XRR results for a tungsten anode deposited under 50 W, 10 mTorr. (a) Reflectivity Data; (b) Fitted Profile	28
Figure 3.4: XRR results for a tungsten anode deposited under 15 W, 3 mTorr. (a) Reflectivity Data; (b) Fitted Profile	30
Figure 3.5: Simulated NR reflectivity plot and SLD profile for a 100 Å thermal silicon oxide and a 150 Å tungsten anode.	32
Figure 3.6: XRR results for a 100 Å thermal silicon oxide and a 150 Å tungsten anode. Courtesy of Dr. Eric Rus, NIST	32
Figure 4.1: EQCM open module schematic.	35
Figure 4.2: Photo of the assembled standard wet cell.	37
Figure 4.3: OCV during NR measurement of the working electrode in a wet cell.	39
Figure 4.4: CV Sweeps after NR measurement	39

Figure 4.5: Plots of current and mass change on a fresh tungsten electrode during CV between 0.05 V and 1.5 V vs. Li/Li+. (a) Current; (b) Mass.....	44
Figure 4.6: Current decay in EQCM cell following SEI growth at an electric potential of 250 mV (vs. Li/Li+), following the 10 CV cycles in Figure 4.2	45
Figure 4.7: NR results for the bare working electrode in helium. (a) Reflectivity Data; (b) Fitted Profile	47
Figure 4.8: NR results for the working electrode after SEI growth, for 0, 1, and 2 surface layer models. (a) Reflectivity data; (b) Fitted profile for 2-layer model; (c) Comparison of fitted profiles of all models	49
Figure 4.9: NR results for a working electrode in electrolyte with no lithium counter electrode. (a) Reflectivity Data; (b) Fitted Profile	52
Figure 5.1: m.p.e values calculated over the reduction sweep for the 1st and 2nd cycles.....	56
Figure 5.2: Histograms of inner SEI component volume fractions	61
Figure 5.3: Histograms of outer SEI component volume fractions	62

LIST OF TABLES

Table 3.1: RMS roughness values (nm) of deposited W films: first optimization round.....	27
Table 3.2: RMS roughness values of deposited tungsten films: second optimization round	27
Table 4.1: Fitted parameters for bare working electrode in helium.....	48
Table 4.2: Fitted parameters for 2-layer model on working electrode after SEI growth.....	50
Table 4.3: Calculated BIC for W1_ocv models.....	50
Table 4.4: Fitted parameters for working electrode in electrolyte with no counter electrode	53
Table 5.1: m.p.e values for common SEI components	55
Table 5.2: Inner SEI Mean Component Volume Fractions	60
Table 5.3: Outer SEI Mean Component Volume Fractions.....	60

ACKNOWLEDGEMENTS

First and foremost, I would like to thank my advisor, Dr. Steven DeCaluwe, for his invaluable guidance and unending patience over the last two and a half years, without which I would have most certainly been lost in this work. I have learned an incredible amount from you, and I am sure to find it helpful in the future.

I would also like to thank my thesis committee, Dr. Robert Kee and Dr. Jason Porter, for taking the time to review my work. Particularly, I am thankful to Dr. Kee for his generous assistance in funding the project when delays caused it to extend past the expected time.

There are also many other scientists and faculty who contributed to the project, in particular Dr. Joseph Dura and Dr. Eric Rus from NIST. Your assistance and insights with neutron reflectometry and data analysis were invaluable, and it is quite safe to say this work could not have happened without you. I would also like to thank Harrison Wilterdink, Rex Rideout, Jim Johnson, and Ellen Verkler, who helped me get trained on various machines and techniques here at CSM. There are other faculty too numerous to name who assisted me in various ways; to all of you, thank you so much for your time.

To the whole thermal sciences group, this would have undoubtedly been a duller experience without you. Thank you for your companionship, advice, and late-night semester project sessions.

I would also of course like to thank my family, who supported me behind the scenes both emotionally and financially. After all, they were the ones who suggested I pursue a graduate degree in the first place.

Finally, I would like to thank the Office of Naval Research and program manager Michele Anderson for funding this project, via grant N000141410059.

CHAPTER 1

INTRODUCTION

Lithium-ion batteries are an increasingly common energy storage device, particularly for portable electronic devices such as cell phones and laptops. This is primarily due to their high energy density and high operating cell voltage compared to other rechargeable battery technology such as NiCd. Recently, lithium-ion batteries have seen higher demand in electric vehicles due to an increasing need for environmentally friendly energy in automobiles [1].

Despite their utility in energy storage, lithium-ion batteries currently face a number of durability and safety issues. Central to many of these issues is the durability of the solid electrolyte interface (SEI), an interfacial layer that forms on the anode during battery charging [1], [2]. While the large voltage window is an attractive feature of lithium-ion batteries, contributing to high energy and power densities, there are currently no suitable electrolytes which are stable over this window, which leads to electrolyte degradation at very high and very low voltages [3], [4]. Electrolyte formulations have been developed in which the degradation products deposit as a film on the anode surface. This film (the SEI) is an ion conductor but is electronically insulating, which enables continued battery operation while passivating the electrolyte from further degradation. While the SEI is therefore, in theory, self-limiting and a necessary step for long battery lifetimes, in reality continued SEI growth and electrolyte degradation during extended battery cycling significantly impacts battery durability, leading to capacity fade (a reduction in the total charge held by the battery), reduced charge/discharge rates, and eventual battery failure [1], [5], [6].

SEI degradation is also associated with a significant safety risk, due to exothermic degradation reactions which can contribute to thermal runaway events that lead to catastrophic battery fires. Damage to the separator between the anode and cathode, either from external trauma or internal defects such as dendritic Li growth or preexisting impurities, can cause the battery to short-circuit. Local heating from this short-circuit can then cause the SEI to undergo exothermic decomposition; the heat from these decomposition reactions can, in turn, trigger additional exothermic reactions, leading to a cascade of exothermic events dubbed “thermal runaway” [7], [8]. At elevated operating temperatures, pressure buildup within the battery can cause the battery casing to fail, allowing superheated flammable electrolyte vapors to escape which then combust in contact with an oxygenated environment [9]. Prominent battery failures have been recorded in products from companies such as Tesla, Boeing, and more recently, Hoverboard Technologies. Though rare, such incidents are catastrophic enough to damage the reputation of both the company and lithium-ion battery technology as a whole.

Methods exist to engineer the SEI for enhanced durability or to minimize thermal decomposition and mitigate thermal runaway and damage from battery failures [10]–[12]. Regardless, the chemistry behind the SEI layer’s formation, evolution, and degradation with age or localized heating remains poorly understood, which inhibits the “rational design” of a durable SEI. With a more thorough understanding of these electrochemical processes, research could focus on directly mitigating or preventing problematic SEI degradation reactions, which would significantly aid in the design of durable and safe lithium-ion batteries.

However, study of the SEI across a range of conditions has been hindered by inadequacies in many common characterization techniques. Due to the thin nature of the SEI and the sensitive chemical environment in which it is formed, SEI chemistry require an *in operando*

technique that is both capable of spatially resolving the SEI and is sensitive to SEI components. Neutron reflectometry (NR) has been shown to be an effective *in operando* technique for SEI characterization. This work focuses on refining this technique and combining it with complementary electrochemical techniques and mass uptake measurements via quartz crystal microbalance with dissipation monitoring (QCM-D) to create a quantitative understanding of the chemo-physical SEI structure.

1.1 Background

This section contains background information regarding lithium ion battery materials and operation, as well as a literature review of existing SEI knowledge via studies using traditional surface characterization techniques.

1.1.1 Device Operation and Material Choices

Lithium-ion batteries are a rechargeable electrochemical energy storage device that shuttles lithium ions between the anode and cathode. Figure 1.1 provides a visualization of this process. During charge, an external voltage is applied to the battery to move lithium ions through the electrolyte from the cathode to the anode, where they intercalate into (or otherwise react with) the anode. The opposite process occurs during discharge [13]. Modern commercial cathodes are typically composed of a lithium metal oxide such as lithium cobalt oxide (LiCoO_2) or lithium manganese oxide (LiMn_2O_4) [14]. While lithium metal itself appears at first glance to be a sensible choice as an anode, its high reactivity and tendency to form dendrites can limit the battery's lifetime at high charge/discharge rates [15]. Therefore, graphite is the most common anode choice due to its availability, safety, and stability. Silicon has been considered as an anode material due to its vastly superior gravimetric capacity, but as silicon expands in volume by nearly 400% during lithium insertion, mechanical integrity issues have prevented its use in

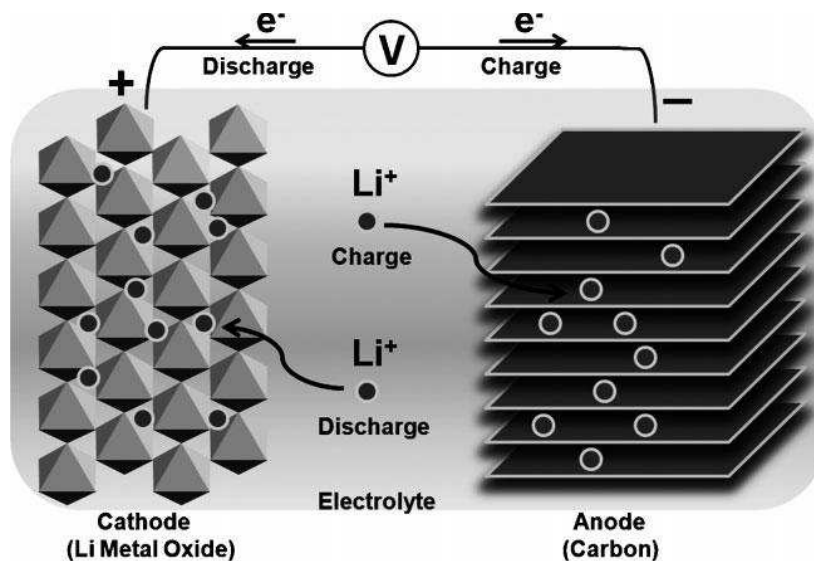


Figure 1.1: Lithium-ion battery operation. *Adopted from Teki, R. et al. Nanostructured Silicon Anodes for Lithium Rechargeable Batteries, 2009 [16].*

commercial batteries [16]. The electrolyte for a lithium-ion battery must exhibit high ionic conductivity, low electronic conductivity, and high electrochemical stability with the electrode materials over the expected operating temperature and potential ranges [4], [17]. Because there are currently no known aqueous electrolytes that adequately meet these criteria, nonaqueous electrolytes are exclusively used. Electrolytes for commercial batteries typically use a mixture of organic solvents such as propylene carbonate (PC), ethylene carbonate (EC), dimethyl carbonate (DMC), diethylene carbonate (DEC), and ethylmethyl carbonate (EMC) due to their low viscosity and ability to form a passivating SEI that protects the electrolyte from excessive reduction [4]. The typical electrolyte formulation combines a linear carbonate (DMC, DEC, or EMC) – which displays superior transport properties but makes for an SEI with rather low stability – with a cyclic carbonate (typically EC, although PC has been explored extensively) – which has poorer transport properties but forms a more stable SEI.

The most popular salt for commercial batteries remains lithium hexafluorophosphate (LiPF_6) for its high ionic conductivity, low viscosity, and its ability to form a stable, passivating SEI. However, it is relatively expensive, has poor thermal stability, and is reactive to trace moisture, requiring the use of highly pure solvents to avoid formation of HF through hydrolysis [18]. For these reasons, other salts have been extensively studied, such as LiClO_4 , LiBF_4 , and LiAsF_6 ; none have seen commercial success due to performance and safety concerns [19]. Recently, LiBOB has attracted attention as a strong candidate as it shares the high conductivity and electrochemical window of LiPF_6 ; furthermore, it has been shown to be less toxic, less expensive, and more thermally stable. However, while stable, the SEI formed in LiBOB cells tend to be very thick, which increases impedance at the anode surface and decreases overall performance [17], [20]. This is related to the difficulty in producing high-purity LiBOB, leading to the reduction of oxalate esters during charging, which is correlated with low efficiency [10], [21].

1.1.2 The Solid Electrolyte Interphase

Due to the large operating potential window of lithium-ion batteries, it is a formidable challenge to find an electrolyte that exhibits good performance and cycling characteristics while simultaneously retaining electrochemical stability over the whole window; this stability window is graphically represented in Figure 1.2. Therefore, during a charge where the cell is brought to low potentials outside the stability window of the electrolyte, the electrolyte decomposes via reduction reactions [1], with the reduction/decomposition products deposited on the anode surface as the SEI. As mentioned previously, the formation of an SEI is linked to a capacity fade in the battery. Therefore, an ideal SEI is compact and chemically stable, forms quickly, and

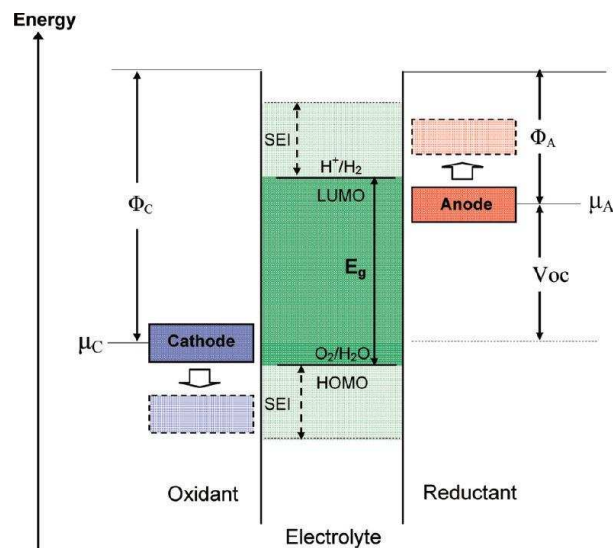


Figure 1.2: Schematic showing the electrochemical stability window for an electrolyte. Φ_A and Φ_C are the work functions for the anode and cathode. Adopted from J. B. Goodenough and Y. Kim, *Challenges for Rechargeable Li Batteries*, 2010.

passivates the anode against further decomposition of the electrolyte while minimizing impedance to Li diffusion.

The thickness of the SEI layer has been reported to range from less than 10 nm [22], [23] to 50 nm [21], [24]. This discrepancy is in part explained by the difficulty of observing the SEI *in operando*; due to its very thin and chemically sensitive nature, the process of disassembling the battery and preparing the SEI for *ex situ* observation introduces a significant source of ambiguity. Another potential cause for the discrepancy in reported values is the similarity in compositions between the SEI and electrolyte, which can make distinction of the boundary between the two difficult. A dual-layer structure to the SEI has been proposed, with a thin, dense, rigid sublayer that forms during initial cycling and a thicker, porous, softer outer layer [25]. The dual-layer structure has been observed in several computational studies, and several possible mechanisms have been put forth. Jorn et al. [26] found that the organic and inorganic

components underwent thermodynamically favorable phase separation, particularly at high inorganic concentrations, and Kim et al. [27] proposed a decomposition mechanism for organic compounds in reaction with lithium near the anode surface. This dual-layer model has also been supported by experimental results, including ion mass spectrometry, quartz crystal microbalance, TEM, and XPS [28]–[30]. An AFM study from Zheng et al. [31] confirmed that the inner layer is rigid and the outer layer is softer, and also observed that the softer outer layer partially dissolved during charging cycles.

While the SEI composition is not fully understood, the composition and properties of the SEI have been found to be highly dependent on the electrolyte [21], [32]. While reduction of electrolyte species is observed to begin at 2.0 V vs Li/Li⁺ [33], the onset potential of bulk SEI formation is often accepted to begin between 0.8 V and 1.0 V vs Li/Li⁺, where decomposition of EC and PC to carbonates (ROCO₂Li) takes place [33], [34]. However, studies have shown that the dense sublayer is primarily composed of inorganic compounds [30]. Lithium carbonate (Li₂CO₃) is a commonly reported component in this layer, as is lithium fluoride (LiF) in electrolytes with fluorinated salts like LiPF₆ and LiBF₄ [28], [35], [36]. One possible explanation for the lack of organic compounds in this initial layer is their tendency to react with trace moisture in the electrolyte to form Li₂CO₃ or trace HF to form LiF and LiOH [32], [37]. Li₂CO₃ has been observed to be a stabilizing component [30], [37], but LiF is believed to have poor conductivity for Li ions [32], [35]. Therefore, for systems with fluorinated salts, high Li impedance in the SEI can significantly affect battery performance.

Studies regarding the evolution and behavior of the SEI at elevated temperatures are comparatively sparse. A number of differential scanning calorimetry (DSC) studies have shown that cycled graphite anodes in a LiPF₆-based electrolyte exhibit the highest thermal response at

temperatures above 250°C [8], [38], [39], but other studies report significant exothermic behavior at temperatures as low as 60°C [12], [40], [41]. This is likely due to the thermal decomposition of the LiPF₆ salt; TGA experiments showed that LiPF₆ loses 60% of its solid mass over 200 minutes at 70°C [42]. Choi et al. [8] suggests that this decomposition leads to the formation of both HF and PF₅ gas, both of which readily react with SEI components.

The low thickness of the SEI, combined with its high reactivity towards oxygen and moisture, can make characterization of the SEI difficult. XPS and FTIR are among the most commonly used characterization techniques, and are often used together due to their complementary nature [2], [21], [24], [34], [39]. Nuclear Magnetic Resonance (NMR) spectroscopy is another frequently used technique, which is sensitive to compounds like LiF that are difficult to quantify with FTIR [43], [44]. However, there are many limitations to traditional surface techniques in studying SEI layers. X-ray techniques have low sensitivity to the light elements that dominate SEI composition, interpretation of FTIR analysis for quantitative composition profiles can be difficult as SEI components are often in overlapping functional groups, and NMR lacks the spatial resolution needed to fully characterize the structure. *Ex situ* studies as a whole have limited utility as the thin, fragile, and reactive nature of the SEI make non-destructive isolation of the SEI difficult. *In situ* and *in operando* techniques are therefore highly preferable, but absorption by the electrolyte and heavy electrode materials still poses a formidable challenge, particularly for x-ray and electron techniques.

1.2 Project Objectives

While traditional *in situ* and *ex situ* techniques have had limited success in SEI characterization, neutron reflectometry has been shown to be an effective tool in SEI characterization due to its sensitivity to elements with low electron density (in contrast to X-ray

techniques), its high spatial resolution, and non-destructive nature [45]–[50]. This is a promising technique that is believed able to probe the SEI structure under a range of conditions, including at a range of electric potentials, in a range of electrolyte chemistries, and at elevated temperatures. Although initial NR results show an ability to measure the SEI thickness and estimate its composition in a range of conditions and on a range of anode materials [45], [50], the initial studies have, for various reasons, lacked the sensitivity for true *quantitative* insight into the SEI chemistry. Therefore, the NR technique requires further refinement to improve its sensitivity to the SEI for a range of studies critical to the design of durable and safe SEI layers. In this thesis, we study the SEI as formed on a non-intercalating thin-film anode by enhancing the sensitivity of the NR technique and coupling it with complementary *in operando* measurements (QCM-D and CV). The use of a non-intercalating anode enhances the sensitivity to subtle shifts in the SEI by isolating all significant structural changes to this layer, and is justified by previous studies which establish that the SEI grown on nonintercalating substrates at low potentials is a suitable approximation of that grown on graphite in Li salts [51], [52].

The specific objectives for this study are as follows:

1. Improve sensitivity of NR to the SEI by using a non-intercalating anode with low neutron scattering contrast with the other battery materials, and develop the fabrication techniques to grow thin films of this material suitable for NR.
2. Use electrochemical QCM-D (EQCM-D) measurements and a suite of complementary electrochemical measurements to characterize SEI growth on the thin-film anode chosen in objective #1.

3. Use *in operando* NR measurements of the newly optimized electrochemical cells to measure chemo-physical SEI structure during its initial formation.
4. Combine the EQCM-D and NR data to build both a physical and chemical understanding of the SEI formation chemistry.

Tungsten is identified as an optimal non-intercalating anode for this study, and is found to significantly enhance sensitivity of NR to the SEI, allowing better resolution of subtle SEI features than previously possible. In particular, this increased sensitivity allows us to make one of the first direct *in operando* measurements of the dual-layer structure outlined in section 1.1.2. The combined EQCM-D and NR data also allows us to perform a detailed quantitative uncertainty analysis of the SEI composition, something which has previously not been explored in any detail. A quantitative compositional understanding is critical for “rational” SEI design efforts, both to understand which chemical reaction pathways are relevant to SEI performance characteristics and to evaluate and compare the SEI across a variety of operating conditions.

CHAPTER 2

EXPERIMENTAL TECHNIQUES

This section will provide a detailed overview of the theory of operation for the various techniques used in this study, as well as their applications to SEI characterization.

2.1 Neutron Reflectometry

The centerpiece of this study is the application of neutron reflectometry (NR) as an *in-operando* technique to study the SEI layer chemistry, which provides unprecedented sensitivity to the SEI thickness and scattering length density (SLD, which is related to its composition) for unaltered SEI layers formed *in operando* on model thin-film electrode surfaces. The following section will outline the principles of NR and the advantages it offers over other, more traditional surface techniques for this study.

2.1.1 Principles of Operation

Neutron reflectometry is a surface characterization technique that scatters an incident beam of highly collimated neutrons off of a sample surface and measures the intensity of the reflected neutrons as a function of the incident angle θ . Incident neutrons will reflect off of interfaces between any layers in the sample, and in a process similar to Bragg diffraction, the path length traveled by the neutrons will vary depending on which interface they reflect off of. Because of the wave-like properties of neutrons, the neutron beam can be collimated such that all of the incident neutrons are of the same wavelength and in-phase. As they reflect off of the different interfaces in the sample, they can move in and out of phase and will constructively and destructively interfere. The path length difference between one interface and the next is dependent on the incident angle θ , and therefore as θ is varied, the reflected neutrons will move

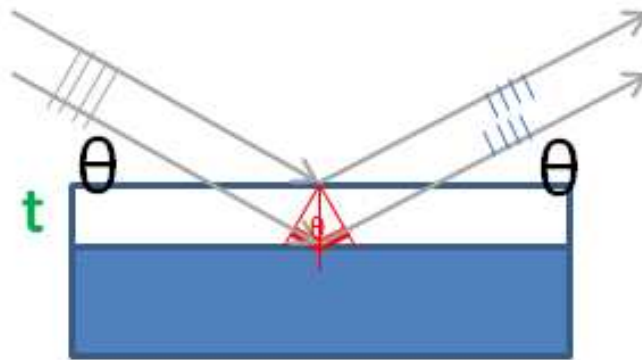


Figure 2.1: Graphic demonstrating how path length differences cause phase shifts in reflected neutrons. Courtesy of Dr. Joseph Dura, NIST.

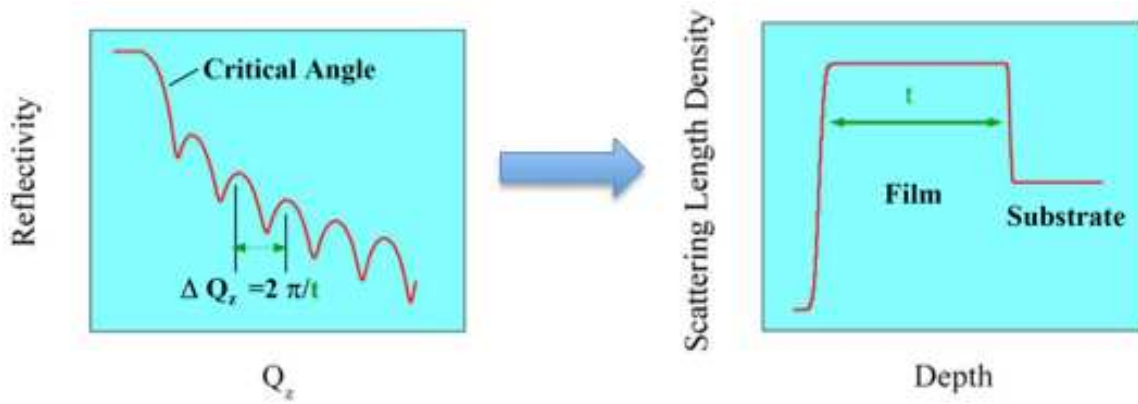


Figure 2.2: Graphic showing the inverse relation between layer thickness and Kiessig fringe period. The raw reflectivity data can be fitted to obtain a more intuitive fitted SLD profile. Courtesy of Dr. Joseph Dura, NIST.

in and out of phase with one another, giving rise to periodic oscillations in the reflected intensity, known as Kiessig fringes. Figure 2.1 and Figure 2.2 provide a visualization of this phenomenon.

Conventionally, rather than use the incident angle θ , the scattering vector Q_z is used, which is the difference between the incident momentum and the reflected momentum vectors of

the neutron beam. For elastic collisions (reflected angle = incident angle), a simple relationship between θ and Q_z can be written:

$$Q_z = \frac{4\pi \sin\theta}{\lambda} \quad (2.1)$$

where λ is the wavelength of the neutron. As Bragg's Law is given as:

$$n\lambda = 2d\sin\theta \quad (2.2)$$

where d is the distance between two interfaces and n is a positive integer, it is easy to see that the periodicity of the Kiessig fringes, ΔQ_z and d are inversely proportional. As the reflected intensity is typically plotted as a function of Q_z , thicker layers will lead to shorter oscillations in Q_z and thinner layers will lead to broader oscillations.

The reflected intensity is not only a function of the thickness of the layers, but also the scattering potential of each layer. The scattering potential for a given layer is a function of both the isotopes in the layer and their density, and is referred to as the scattering-length density (SLD). For a layer made up of isotopes k with a known number density n_k [e.g. molecules/Å³], and scattering length b_k (which are known and tabulated for all isotopes and have units of Å/molecule) the SLD can be calculated as:

$$SLD = \sum_k b_k n_k \quad (2.3)$$

If multiple phases are present in a layer i , the SLD of the layer, SLD_i can also be calculated as a volume average of each of the phases j :

$$SLD_i = \sum_j V_j SLD_j \quad (2.4)$$

where the SLD_j can be calculated according to eq. 2.3. Therefore, the goal of any NR study is to take the reflectivity data and extract from it a 1-D depth profile of the SLD of the thin film structure, as shown in Figure 2.2. This yields layer-by-layer information about the thickness and

composition of the structure, and can do so with sub-Angstrom precision for layers at the nanoscale.

2.1.2 Advantages of Neutron Reflectometry

While NR is similar in principle to other, more common techniques such as x-ray diffraction, it has some important advantages. X-rays yield information about sample structure by interacting with an atom's electron cloud, and therefore x-ray techniques are inherently more suitable for studying heavy, high-Z materials. They are less sensitive to light elements (such as Li or H), especially in the presence of heavier ones. In addition, due to the high energy of x-rays, great care must be taken to ensure that the x-ray probe does not affect the sample being characterized, particularly for thin and sensitive layers. Neutrons, however, yield information by interacting with the nucleus of atoms, and can therefore be sensitive to light and heavy elements alike. This also causes neutrons to be both highly penetrating and non-destructive in nature. Furthermore, because neutrons interact with the nucleus, the neutron scattering cross-section b_k can vary significantly between different isotopes of the same element (the contrast is particularly strong between isotopes of H and Li), making it possible to precisely determine the depth profile and chemical source of these elements.

These qualities make NR quite suitable for *in operando* study of SEI layers, which are typically composed of light organic compounds and lithium compounds. The non-destructive property of NR means that the relatively delicate SEI will be unaffected by the measurement, and the penetrating power of neutrons eliminates the need for a "window" to the SEI through the electrochemical cell during *in-operando* measurements, greatly simplifying the experimental setup.

2.1.3 Challenges of Neutron Reflectometry

In spite of its myriad advantages, NR has several challenges that must be addressed, the most obvious being its cost. X-rays are easy to produce, and most institutions will have x-ray machines available. In contrast, neutrons are typically produced in nuclear reactors, particle accelerators, or spallation sources, which are expensive to construct and maintain and are typically housed at federally-funded national labs and user facilities. Due to the limited availability of neutron sources, there is much competition for time on neutron equipment. To expound on this problem, the intensity of neutron beams are typically several orders of magnitude lower than x-ray beams, making neutron experiments a lengthy process, sometimes on the order of 12 hours or more for a single spectra. Therefore, neutron experiments must be carefully planned to be able to collect sufficient data in the limited available timeframe.

Additionally, the process of extracting the SLD profile from reflectivity data is not a trivial task. While mathematical methods exist to convert an SLD profile to a theoretical reflectivity, the inverse is not true. There is no way to mathematically calculate a single SLD profile from reflectivity data; this is because the reflected intensity is measured, rather than the neutron wave vector itself. Therefore, in order to extract the SLD profile, the “inverse problem” must be solved, via fitting algorithms that find an SLD profile whose theoretical reflectivity matches the experimental data.

Once the most likely SLD profile is determined, converting this to a chemical composition can also be a difficult process. Using either eq. 2.3 or 2.4, one can see that for a layer with more than two components, the fitted SLD profile is not a unique function of the composition (e.g., using eq. 2.4, there are more than two unknowns – the volume fractions - but only two equations – eq. 2.4 and the requirement that all volume fractions sum to 1). It is

therefore important to have some prior knowledge of the structure and composition of the sample in order to narrow down the pool of potential solutions to a finite set of physically sensible candidates. In the case of multiple competing fits that are physically sensible, complementary data from other experiments may be required to choose a fit. Alternatively, because of the sensitivity of NR to different isotopes of an element, it is possible to exchange a layer with an otherwise chemically identical isotope and take additional NR data. For example, it is possible to measure two SEI grown in identical conditions - once in a protonated and once in a deuterated electrolyte. This technique ('isotope contrast variation') can help discriminate between competing SLD profile fits [53], can directly measure the depth profile of H number density with high precision, and therefore adds an additional constraint equation to any composition model.

Finally, it is important to note that while any given substance has an absolute value for its SLD, NR is not sensitive to this exact value. Rather, it is sensitive to a layer's SLD relative to the SLD of adjacent layers. The larger the difference in SLD between two layers, the more that interface will contribute to the shape of the reflectivity plot. Therefore, it can be difficult to resolve layers that have low SLD contrast with adjacent layers, especially in the presence of large contrasts elsewhere in the structure.

2.1.4 Fitting NR Data

Because there is no method of directly calculating the SLD profile from reflectivity data, it is instead determined by generating possible SLD profiles, calculating their theoretical reflectivity, and evaluating how well they fit the data. Commonly, candidate SLD profiles are calculated by considering a model that treats each material layer in the profile as a 'slab' with three parameters: thickness, SLD, and interfacial width (e.g. roughness or composition gradients) at the adjacent layer. Prior knowledge of the film can aid in fixing or bracketing the number of

layers and some of the layer parameters, decreasing both the computational time and the chance of obtaining unphysical fits.

Fitting for simple structures can be done quickly using basic gradient-descent algorithms, but this method is often unsuited for complex, many-parameter fits; for these cases, gradient-descent methods are prone to getting caught in local minima, and also cannot directly determine the correlation between fitting parameters, which is required for accurate error estimates of the fitted parameters. In this study, Refl1D [54], a software package developed at NIST and the University of Maryland as part of the DANSE project, is used to fit the NR data. The program is described in greater detail in DeCaluwe, et al. [53], but briefly, the program uses a differential evolution algorithm (DREAM) to generate a random collection of parameter sets from the entire parameter space. The program then allows the population of fits to “evolve” with a user-defined number of generations, using a “survival of the fittest” algorithm (with fitness judged according to the χ^2 metric).

While this approach is slower than gradient-descent approach, it can more reliably locate the global minimum of the identified parameter space than these commonly used methods. Additionally, this approach is able to find correlations between parameters, where changes to one parameter affects the best fit value for another; this can indicate the suitability of the proposed model by identifying when fitted parameters are dependent and better formulated as part of a separate parameter. Finally, because of the statistical nature of the underlying genetic algorithm, it is possible to make a detailed uncertainty analysis, factoring in parameter correlations into uncertainty estimates for the fitted parameter values.

Because the inclusion of additional parameters typically improves the goodness-of-fit (χ^2), it is important to prevent overfitting, i.e. creating unnecessarily complex fitted profiles with too

many degrees of freedom that may return good χ^2 values despite being clearly unphysical. Therefore, in this study, fitted profiles are evaluated using the Bayesian Information Criterion (BIC), a method of calculating the goodness-of-fit that penalizes large models. The BIC is calculated as thus:

$$BIC = (n - k) * \ln(\chi^2) + k * \ln(n) \quad (2.5)$$

where k is the number of parameters and n is the number of data points being fitted. Fitting therefore seeks to minimize BIC, and a difference in BIC of 10 or greater between two models is generally seen as compelling evidence against the weaker model [62].

2.2 Electrochemical Quartz Crystal Microbalance with Dissipation Monitoring

As explained previously in Chapter 1, despite NR's promise as an *in operando* probe, the non-unique relationship between SLD and composition (i.e. different layer compositions can, in theory, give the same SLD) limits the ability of NR to definitively quantitative the SEI's chemical composition. To build a more complete picture of the SEI, it is therefore necessary to complement the NR data with other *in operando* experiments. Additionally, because of the limited availability of neutron facilities, it is useful to screen a range of possible conditions with more readily available techniques and choose only the most relevant conditions for NR. For this study, a combination of quartz crystal microbalance (QCM) and a suite of simultaneous electrochemical measurements will be used to support the NR data. The following section will provide a brief background of QCM and the various electrochemical techniques, and their application to this study.

2.2.1 Quartz Crystal Microbalance with Dissipation Monitoring

QCM is a technique used to measure mass changes corresponding to the chemical processes (film growth or dissolution, absorption, and other chemical reactions) of a film on the

surface of a quartz crystal sensor by measuring the change in the sensor's resonant frequency. As quartz is a piezoelectric material, applying a sinusoidal voltage input across a quartz crystal sensor causes it to vibrate. By linearly sweeping the frequency of the alternating current, it is possible to measure the resonant frequency of the sensor, typically in the 5-6 MHz range, to a precision within 1 Hz. The resonant frequency is dependent on the mass of the crystal, and so by continuously monitoring the resonant frequency of the sensor, the mass of a film grown on the sensor's surface can be measured with a resolution on the order of ng/cm². Figure 2.3 shows the effect of a deposited mass on the measured frequency.

For most systems, it is acceptable to use the Sauerbrey equation to relate the change in frequency to the change in mass, which is given as:

$$\Delta f = -\frac{2f_0^2}{A\sqrt{\rho_q\mu_q}}\Delta m \quad (2.5)$$

where f_0 is the resonant frequency of the sensor, A is the sensor area, and ρ_q and μ_q are the density and shear modulus of quartz, respectively. This relation assumes that the deposited film is rigid and the relative change in frequency to the resonant frequency is less than 2%. While the above formulation assumes operation in air, it can be generalized to operation in liquid by applying an initial viscosity-related correction factor to the frequency change.

For softer films, the resonant frequency is a function of both the mass and the viscoelasticity of the film on the sensor surface, and the Sauerbrey relation does not hold; a more complex model must be used. Voinova et al. [56] formulated such a model, commonly known as the viscoelastic model, which uses the film's density and complex shear modulus as additional fitting parameters. To accomplish this, the energy dissipation during oscillation is measured

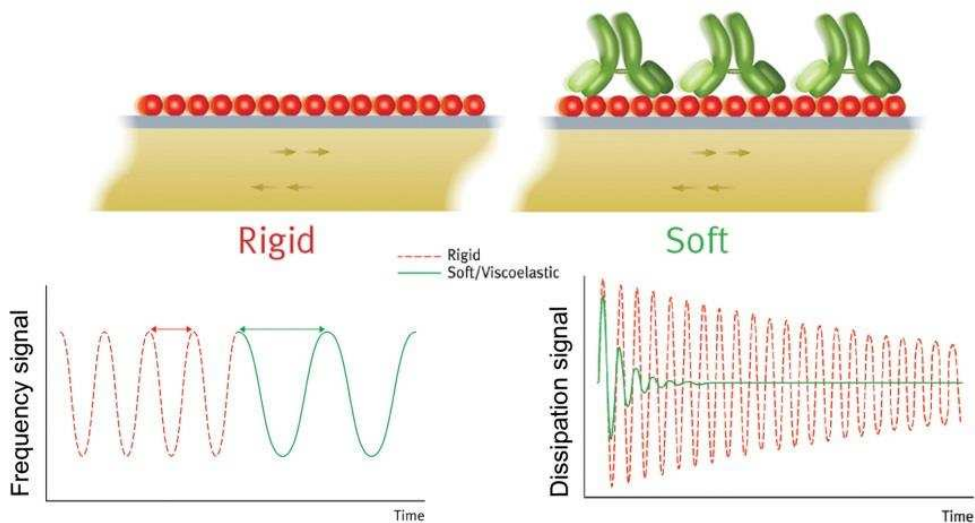


Figure 2.3: Demonstration of the effect of both rigid and elastic layers on the effect of QCM-D data. Adopted from Biolin Scientific, *Quartz Crystal Microbalance*, 2016 [55].

alongside the resonant frequency; this technique is known as QCM with dissipation monitoring (QCM-D). In QCM-D, the oscillating voltage input is terminated, and the decay in the vibration amplitude is monitored, as depicted in the right-hand side of Figure 2.3. By fitting both the frequency (f) and dissipation (D), which are typically monitored at multiple harmonic frequencies in addition to the fundamental, it is therefore possible to monitor both the mass and viscoelastic evolution of the film during experiments. The effect on layer viscoelasticity on the measured dissipation can be seen in the rightmost graph in Figure 2.3.

2.2.2 Electrochemical Measurements

Electrochemical studies involving QCM-D often take complementary electrochemical measurements simultaneously with QCM-D measurements. This is known as electrochemical QCM-D (EQCM-D). For this study, these electrochemical tests are done both to grow the SEI and provide additional information (voltage, current, and impedance) to complement the mass data provided by QCM-D.

Cyclic voltammetry (CV) is a technique that sweeps the potential of a working electrode in an electrochemical system repeatedly between two setpoints and measures the resulting current. The potential is typically swept multiple times to observe how the current changes at a given potential from one cycle to the next. This is commonly used to characterize the behavior of electrochemical systems, and provides information regarding the properties of the various electrochemical reactions that can occur, such as the voltage at which they become thermodynamically favorable, the current magnitude, reversibility, and passivation. For this study, CV is used to simulate multiple charge-discharge cycles for a cell, which grows an SEI on the surface of the QCM-D sensor. It is also possible to use the mass uptake from the QCM-D measurement together with the charge data from CV, obtained by integrating the current as a function of time, to calculate the charge transferred per unit mass at a given potential; this is useful in identifying SEI formation reactions, according to what is deposited on the sensor surface as SEI. This technique, known as m.p.e analysis, has been used previously in similar studies of the SEI [29], [32], [33], and has been demonstrated to be effective in providing information regarding the composition of the SEI. Chapter 5 provides a more detailed analysis using this technique.

Chronoamperometry is a simple technique in which the potential of the cell is held at a constant value and the current is measured as a function of time. The potential can also be stepped to different values to observe the resulting change in current. This can be useful for determining both the kinetic rates of a desired reaction and the total amount of charge that is transferred. In this study, because NR experiments require a static and stable sample, chronoamperometry is used to determine the time required for the SEI electrochemistry to stabilize after growth and measure the total charge deposited into the SEI during growth.

2.3 Conclusion

This chapter provided the principles of operation of EQCM-D and NR and their applications and advantages to SEI characterization. NR will be used to create a 1-D depth profile of the chemical composition and physical structure of the SEI. EQCM-D will be used to characterize the SEI formation and stabilization processes and provide complementary charge and mass data for NR.

In particular, NR is a powerful *in operando* technique that has been shown to be effective in studying the SEI [45]–[50]. We now turn our attention to refining the technique outlined in the literature in order to enhance its sensitivity to the SEI, enabling higher resolution qualitative and quantitative analyses of the SEI.

CHAPTER 3

THIN FILM ANODE FABRICATION

The first-ever use of NR as an *in operando* probe of SEI composition and structure was completed by Owejan, et al. [45]. This study formed an SEI on a thin-film, non-intercalating copper electrode and observed its thickness and scattering potential as a function of electric potential during a series of potentiostatic holds meant to approximate a charge-discharge cycle. The use of the non-intercalating anode eliminated swelling and composition changes in the anode during electrochemical cycling, such that all variations in the NR data were associated with the SEI, thereby increasing the study's sensitivity. Additionally, the EC solvent in the electrolyte was deuterated, thereby increasing the SLD of the electrolyte (deuterium has a higher SLD than hydrogen) and increasing its contrast with the SEI, which is expected to have a low SLD due to the incorporation of Li ($SLD_{Li} = -0.88 \cdot 10^{-6} / \text{\AA}^2$).

While this work as well as subsequent efforts [46], [48]–[50] demonstrate the ability of neutron reflectometry to measure the SEI *in operando*, the effect of an SEI layer on the NR data is typically rather subtle. For example, Figure 3.1(a) shows a comparison between simulated reflectivity plots between a copper anode with and without a surface SEI layer, which is very similar to the measured profiles shown in Figure 1 of Owejan, et al. [45]. Due to the high contrast between the SLD of the copper electrode and the titanium adhesion layer, scattering on this interface is dominant. The relatively weak contrast between the SEI and adjacent layers leads to fairly small changes in the NR data. Therefore, while the SEI is clearly detectable on copper, it becomes difficult to accurately measure subtle changes in its chemistry. To be able to

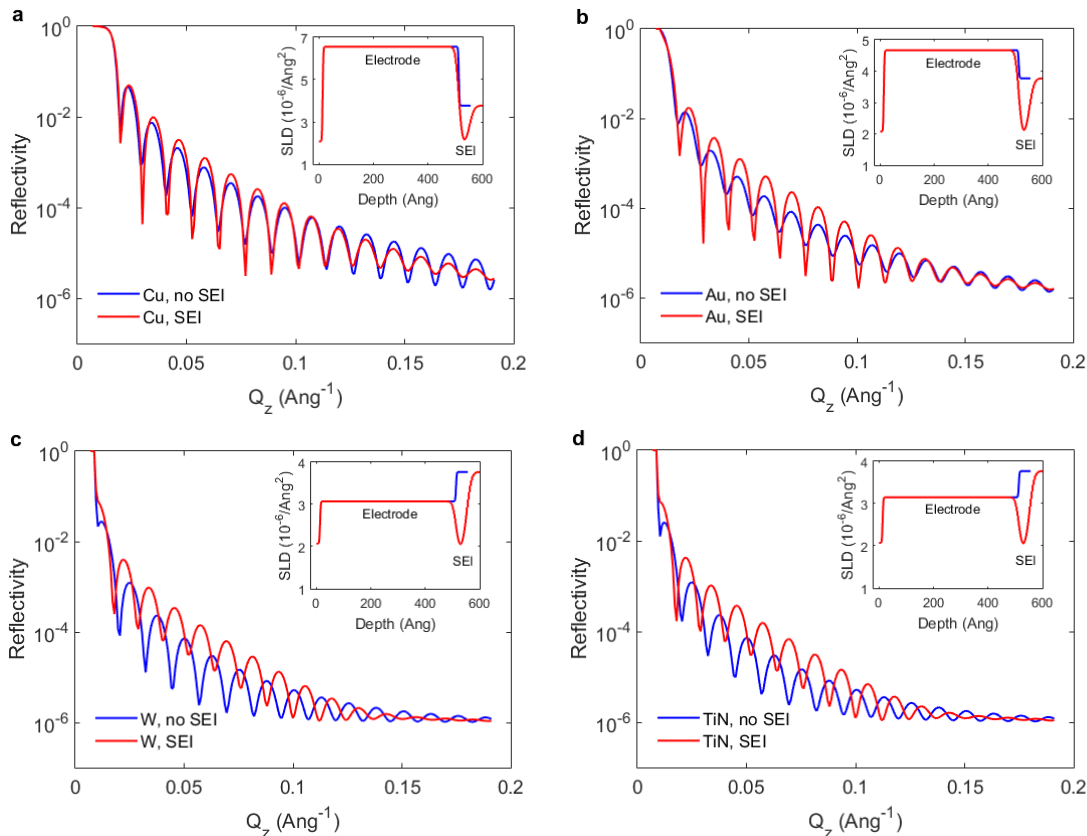


Figure 3.1: Simulated NR reflectivity plots comparing various anode materials with and without an SEI layer. (a) Copper anode; (b) Gold anode; (c) Tungsten anode; (d) Titanium Nitride anode

study an evolving SEI with precision, it is necessary to design a system with higher sensitivity to the SEI.

3.1 Electrode Material Choice

As the primary cause of the previous study's relatively low sensitivity to the SEI is the high SLD contrast between the copper electrode and substrate, choosing an electrode material that has a lower contrast with the adjacent materials (substrate and electrolyte) will boost sensitivity to the SEI. To identify suitable electrode materials for NR study with enhanced SEI sensitivity, NR was simulated for a range of electrode materials (including gold, titanium nitride,

and tungsten) and a range of thicknesses (ranging from 35 - 60 nm). The simulated reflectivities and SLD profiles for 50 nm thick electrodes are shown in Figure 3.1(b)-(d).

In addition to suitable SLD contrast, it is important that the chosen material can be easily fabricated as a thin-film suitable for NR study of the SEI. To enhance the NR sensitivity to changes in the SEI, it is important that all changes to NR data be attributable to evolution of the SEI layer; changes in any of the other layers lead to unnecessary confounding, which can significantly limit NR's power to characterize the SEI. Because silicon stores lithium, it is particularly important that the electrode thin film is dense enough to prevent Li ions from reaching the silicon substrate. Additionally, because the thin SEI layer(s) will lead to broad oscillations in the NR data, measurements must be taken to reasonably high Q_z in order to resolve the SEI. Interfacial roughness in the layers causes dampening of the oscillations, and it is therefore necessary to minimize the surface roughness of the thin film electrode: in this study, high-quality NR data requires a RMS roughness no greater than 2 nm. In choosing an electrode material, it is therefore important to consider our ability to deposit a suitable thin film, as well as the material's scattering properties.

While titanium nitride (TiN) was an initial candidate for the electrode material, as shown by the significant difference in the red and blue NR curves in Figure 3.1(d), finding a deposition process for TiN that yielded smooth and dense thin films adequate for NR study proved a formidable challenge. Tungsten (W) thin films, on the other hand, have wide application in the electronics and semiconductor industries due to tungsten's desirable thermal and electrical properties. The deposition process of tungsten is therefore relatively well understood, and it is known that depositing dense thin films is feasible. Additionally, tungsten shows low SLD contrast with the electrolyte and Si substrate, as seen in the simulated reflectivity plot in Figure

3.1(c), which therefore results in high NR sensitivity to the properties of the SEI. Finally, tungsten does not intercalate lithium or form silicides in contact with silicon at low temperatures [57], minimizing the number of distinct layers and simplifying the fitting process for NR data. Therefore, tungsten was chosen as the electrode material for this NR study.

3.2 Optimization of Tungsten Deposition

While processes have been established for the deposition of dense W thin films, comparatively little data exists in the literature regarding surface roughness, and none could be found exhibiting the required 2 nm RMS roughness for our study. Extensive attention was therefore devoted to optimizing the deposition process to meet the required density and roughness requirements for NR study.

Sample fabrication was carried out using a Semicore DC magnetron sputter system at the Colorado School of Mines (CSM). Sputtering is a physical vapor deposition (PVD) process that applies a voltage bias between a target and a substrate within a low-pressure inert gas environment, which causes gas particles to ionize and strike the target, physically dislodging atoms from the target and causing them to deposit (“sputter”) onto the substrate. As the high melting point of tungsten makes evaporative techniques difficult, sputtering is a relatively simple alternative.

In this study, sputtering was done using a 99.95% W target in a chamber that was pumped down to below 1E-6 Torr before the introduction of ultra-high purity (UHP) argon as a sputtering gas. The W thin films used for this optimization study were deposited onto polished 3” diameter Si wafers. The Si wafers were first cleaned with a μ -90 detergent scrub, rinsed in DI water, blown dry with N₂ gas, and cleaned with a spin-rinse in HPLC-grade ethanol. The wafers were then etched using a dilute 2% HF solution to remove the native oxide prior to deposition.

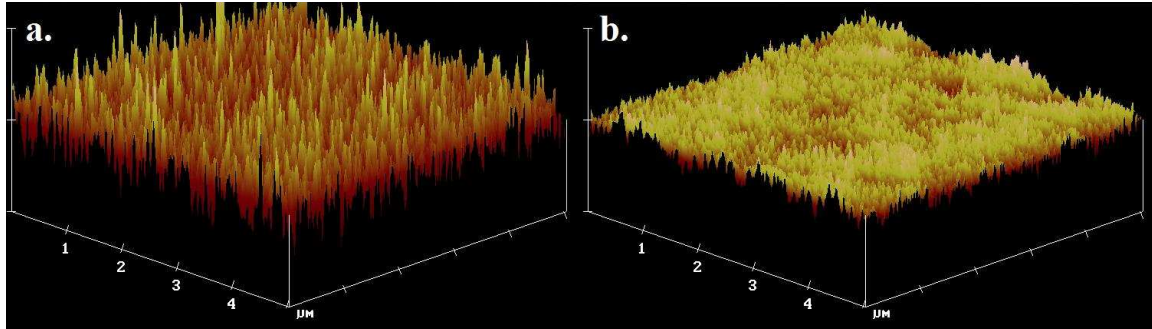


Figure 3.2: 3D plots of AFM scans for a tungsten thin film under different deposition conditions. (a) 50 W, 10 mTorr; (b) 15 W, 3 mTorr

Table 3.1: RMS roughness values (nm) of deposited W films: first optimization round

Power (W)	Ar Pressure (mTorr)		
	5	10	20
50	0.557	0.443	0.486
100	0.812	0.852	1.12
200	1.29	0.732	0.581

Table 3.2: RMS roughness values of deposited tungsten films: second optimization round

Power (W)	Ar Chamber Pressure (mTorr)			
	1	3	5	10
10	0.280	0.358	0.367	0.497
15	0.426	0.224	0.326	0.314

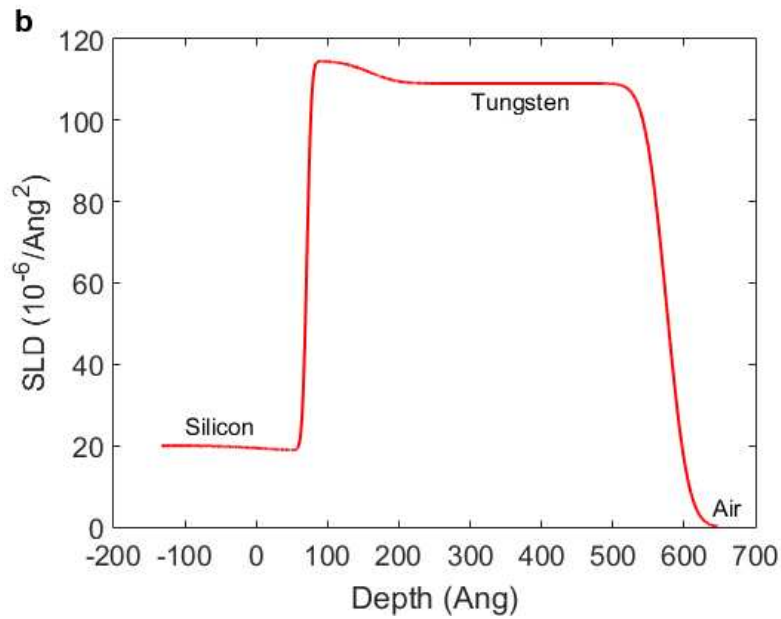
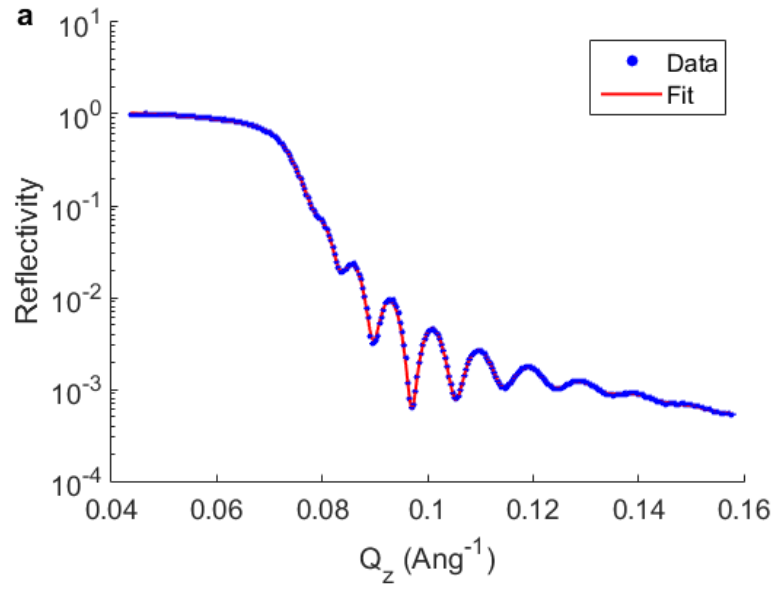


Figure 3.3: XRR results for a tungsten anode deposited under 50 W, 10 mTorr. (a) Reflectivity Data; (b) Fitted Profile

The deposition process established by Watjen [58] was taken as the baseline for the optimization study, and the deposition power and argon pressure were varied to optimize surface roughness. As the thickness of the deposited thin film can affect its surface roughness, deposition rates at each set of conditions were first determined by a step test with a Kapton tape mask using a Tencor P10 profilometer. The sputtering time was then adjusted on each set of deposition conditions to achieve a film thickness of roughly 50 nm. This ensures that differences in the surface roughness are a function of the tested deposition parameters only.

To characterize the surface roughness of the deposited films, initial screening was done using atomic force microscopy (AFM) on a Veeco Dimension 3100 Atomic Force Microscope at CSM with Bruker TESP-V2 probes. These measurements were done in tapping mode to minimize damage to the film surface during scanning. Scans were taken over $5 \mu\text{m}$ squares at a scan rate of 0.2 Hz. As AFM is only able to probe surface roughness over microscopic scales, the best samples from AFM characterization were then sent to the NIST Center for Neutron Research (NCNR) in Gaithersburg, MD to be studied with x-ray reflectivity (XRR) on a Bruker D8 X-Ray Reflectometer. The XRR data was reduced and fit using the ReflPak and Refl1d software packages, respectively.

Table 3.1 shows the RMS roughness values (nm) measured by AFM for the first set of deposition conditions in the optimization study. The smoothest sample, deposited with 50 W and 10 mTorr Ar pressure for a measured roughness of 0.443 nm, was reproduced on a fresh Si wafer with the same deposition parameters, where it was then characterized by XRR at NIST. Figure 3.3 shows the XRR reflectivity and fitted profile for this sample. The oscillations flatten out by $Q_z = 1.6 \text{ nm}^{-1}$, suggesting the sample is too rough for NR, which is confirmed by the fitted surface roughness of 5.6 nm. A 3D plot of the original AFM scan in Figure 3.2(a) shows that the

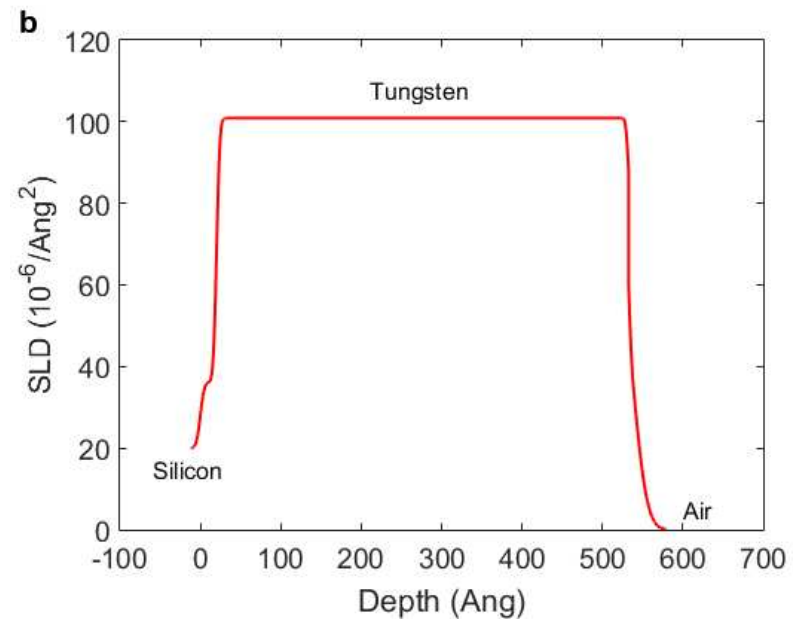
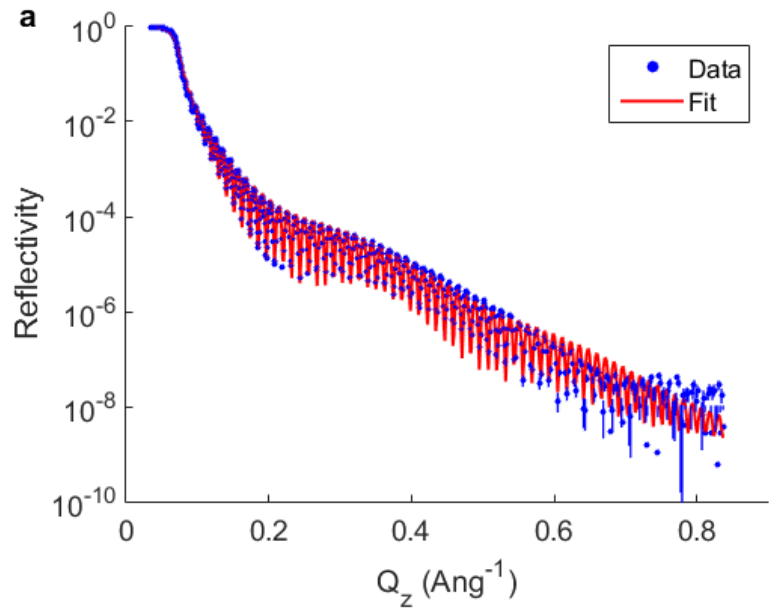


Figure 3.4: XRR results for a tungsten anode deposited under 15 W, 3 mTorr. (a) Reflectivity Data; (b) Fitted Profile

feature size is primarily in the 3-4 nm range, further supporting the XRR results. Given the discrepancy between the measured roughness between the XRR and AFM results, it is possible that the features contributing to the roughness are larger than can be probed with the AFM; it is also possible that the values are calculated differently. Regardless, AFM was shown to be a quick and simple screening technique, but one that requires follow-up via reflectivity study on similarly sized samples.

As porosity and roughness of thin films deposited via sputtering tend to decrease at lower deposition rates [59], the sputtering power and Ar pressure were lowered in the second iteration of the optimization study. Table 3.1 shows the RMS roughness values (nm) measured by AFM for films grown with lower deposition rates, and Figure 3.2(b) shows the 3D AFM surface profile for the smoothest sample, deposited with 10 W and 3 mTorr Ar pressure. This sample was reproduced on a fresh Si wafer and sent to NIST, where Dr. Joseph Dura performed XRR characterization. Reduction and fitting of the XRR data was performed at CSM, and Figure 3.4 shows the reflectivity and fitted profile for this sample. The oscillations on this sample are seen to survive past $Q_z = 7 \text{ nm}^{-1}$, indicating that this sample is much smoother than the previous one. The fit yielded a surface roughness of 1.4 nm, which is adequate for NR study. The profile in Figure 3.2(b) confirms that the features are under 2 nm size, and that the film is considerably smoother than the sample grown at higher deposition rates.

Both of the samples characterized by XRR showed an interfacial layer between the tungsten and silicon, which was required to obtain an acceptable fit. As tungsten silicide is not expected to form under these deposition conditions, this layer may represent trace contamination remaining after cleaning or a native silicon oxide regrown after etching. As the origin of this layer is ambiguous and may therefore introduce unnecessary fitting complexity in NR, a thick

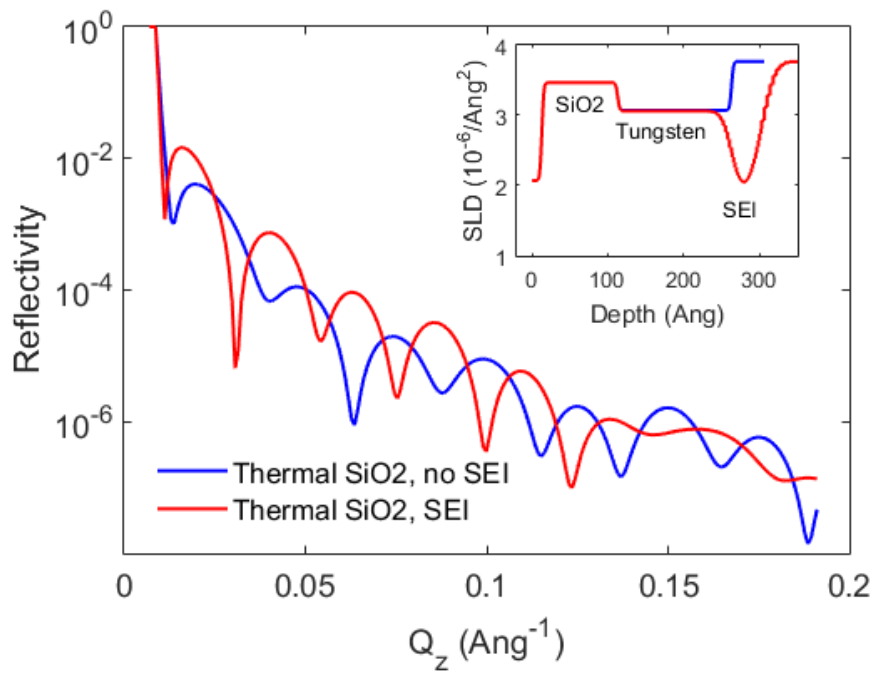


Figure 3.5: Simulated NR reflectivity plot and SLD profile for a 100 Å thermal silicon oxide and a 150 Å tungsten anode.

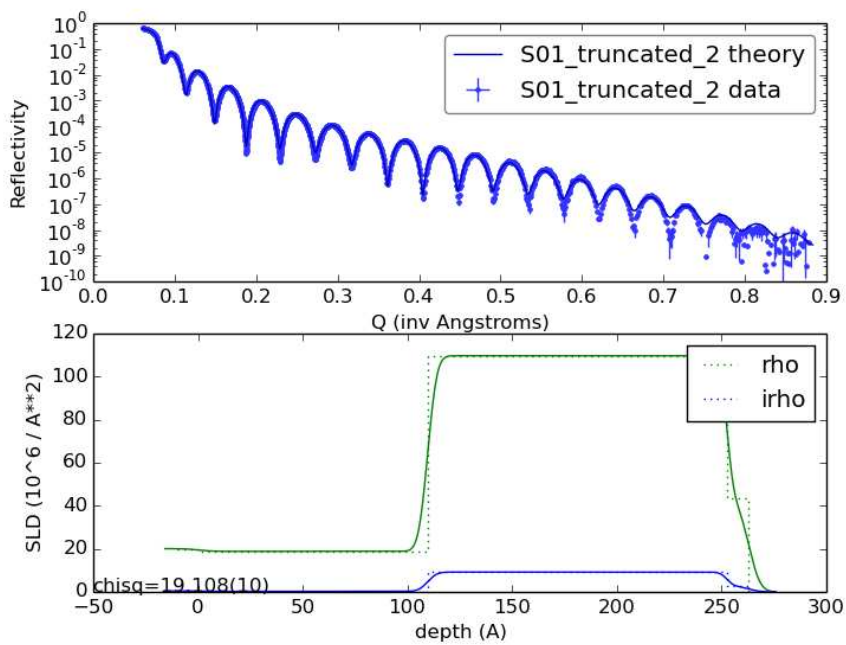


Figure 3.6: XRR results for a 100 Å thermal silicon oxide and a 150 Å tungsten anode. Courtesy of Dr. Eric Rus, NIST

thermal oxide layer was grown on the silicon substrate prior to tungsten deposition. In addition to being a layer with known parameters, a thermal oxide can act as a barrier layer between lithium in the electrolyte and the silicon substrate in the event that electrolyte is able to pass through any residual pores in the tungsten layer. Since an additional layer could potentially affect the NR sensitivity, NR spectra for a range of thermal oxide/tungsten thicknesses were simulated to find the optimal thermal oxide and tungsten thicknesses. This simulation study, along with sample fabrication and follow-up XRR to confirm the surface roughness was still acceptable, was performed by Dr. Eric Rus at NIST. The optimal thicknesses were found to be a 100 Å thermal silicon oxide and a 150 Å tungsten film, and a simulated NR reflectivity plot and follow-up XRR characterization on a fabricated sample are shown in Figure 3.5 and Figure 3.6, respectively.

3.3 Conclusion

In this chapter, we have developed and optimized deposition routines for thin-film non-intercalating electrodes suitable for NR study. While optimizing deposition routines may not be of the highest scientific value, we emphasize here that developing suitable substrates is a critical step in obtaining high-quality NR data. Poorly chosen materials (i.e. poor SLD contrast matching) will make it difficult to isolate the impact of the SEI on the reflectivity data, no matter how good the sample fabrication, while poorly fabricated samples (high surface roughness or high porosity) will result in low-quality data, making it difficult to properly fit the data or even obscuring the SEI entirely (if the roughness is larger than the SEI thickness, it not be resolved as a distinct layer, but rather as an SLD gradient between the electrode and electrolyte SLDs).

Having developed routines for high-quality electrode substrates, the following chapters describe the analysis of the SEI grown on these electrodes, using the *in operando*, multi-modal platform described in Chapter 1 and Chapter 2 (NR, electrochemistry, and EQCM-D).

CHAPTER 4

EXPERIMENTAL RESULTS

This chapter contains the experimental procedures and results for the techniques outlined in Chapter 2. Synthesis and analysis of these results to build a clearer quantitative compositional understanding of the SEI are covered in Chapter 5.

4.1 Materials and Methods

This section contains the facilities, equipment, and experimental procedures for both EQCM-D and NR experiments.

4.1.1 EQCM-D Equipment

QCM measurements are done using the Q-Sense E1 system from Biolin Scientific. The Q-Sense open module is used, which allows direct access to the sensor surface. The QSX312 sensors used in these measurements are 350 μm thick quartz crystals with a resonant frequency of 4.95 MHz. To remain consistent with the NR measurements, the sensors have a tungsten thin film deposited onto the sensor surface to function as a working electrode. Proprietary software provided by Q-Sense is used for viscoelastic modeling.

A Gamry Reference 600 potentiostat is used to control the electrochemical measurements during EQCM-D experiments. A strip of copper adhesive tape is attached to a pin on the bottom of the QCM open module to provide electrical access for the potentiostat to the working electrode. Proprietary software from Gamry is used to control the potentiostat. Figure 4.1 shows a schematic of the EQCM cell.

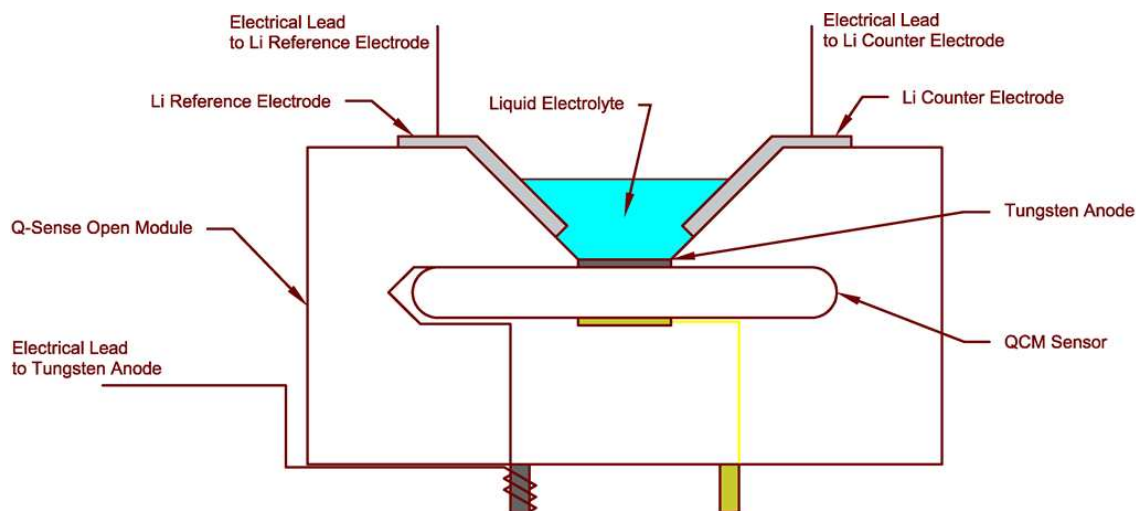


Figure 4.1: EQCM open module schematic.

The electrolyte used in this study is a 1 M LiPF_6 solution in a 1:1 (v/v) mixture of ethylene carbonate (EC) and diethyl carbonate (DEC) as received from Sigma-Aldrich. Lithium foil (Sigma-Aldrich) is used as both the counter electrode and reference electrode. As all of the materials in this study are highly sensitive to oxygen and moisture, all EQCM-D work is done in an argon-filled glove box with O_2 and H_2O levels below 1 ppm.

4.1.2 EQCM-D Experimental Procedure

Prior to SEI growth, the tungsten QCM-D sensor is cleaned by sonication in a 2% sodium dodecyl sulfate (SDS) solution at 40 °C for 30 minutes. The sensor is then rinsed with DI water and blown dry with N_2 gas. The cell in Figure 4.1 is assembled in the glove box, and the baseline resonant frequencies and dissipations for the sensor are calibrated in electrolyte.

Cyclic voltammetry is used to grow an SEI on the sensor surface of the cell in Figure 4.1. 10 sweeps are taken at 10 mV/s between 0.05 and 1.5 V vs. Li/Li^+ at a controlled temperature of 30 °C. The QCM-D module monitors frequency and dissipation during the sweeps. The QCM-D

data is later fit using the viscoelastic modeling software from Q-Sense using the nominal density and viscosity of the electrolyte (1.26 g/cm^3 and $3.4 \times 10^{-3} \text{ kg/ms}$, respectively) as parameters.

After cycling is complete, a chronoamperometry experiment at a potentiostatic hold of 250 mV is done on the cell to predict the amount of time required for the SEI electrochemistry to fully stabilize after growth.

4.1.3 Neutron Facilities

The neutron source used in this study is a 40 MW nuclear reactor at the National Institute of Standards and Technology (NIST) in Gaithersburg, MD. NR is done using the Multi-Angle Grazing-Incidence K-vector (MAGIK) Off-Specular Reflectometer located in the NIST Center for Neutron Research (NCNR). This instrument uses a beam with a wavelength of 5 \AA .

4.1.4 NR Measurement of As-Grown Electrode

Before growing the SEI, the working electrode structure in contact with vapor was measured via NR in order to gain an understanding of the substrate before any electrochemical activity. This provides additional data that can be used in conjunction with NR after SEI growth to simplify the fitting process. The working electrode was isolated in a sealed aluminum can in a helium-filled glove box to avoid both contamination from particulates in the atmosphere and oxidation of the tungsten thin film. NR data was then collected for scattering vectors ranging from $0.008 \leq Q_z \leq 0.03 \text{ \AA}^{-1}$, as shown in Figure 4.7. This data set will be referred to as ‘W1_bare’ (tungsten sample #1, measured as grown [bare] in vapor).

4.1.5 NR Measurement of the Battery Cell at OCV

Following measurement in vapor, sample W1 was removed from the Al can and installed in the NR-compatible electrochemical cell, an example of which is shown in Figure 4.2. The cell

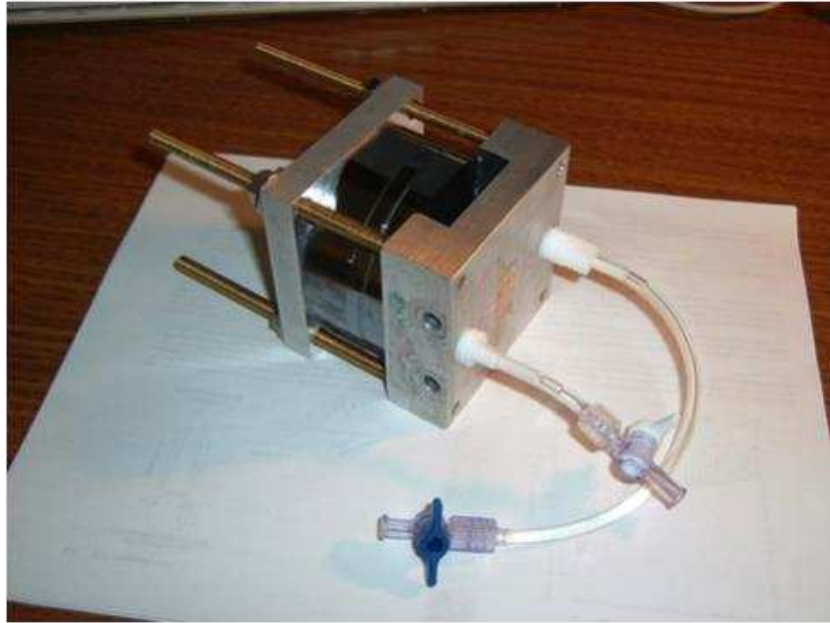


Figure 4.2: Photo of the assembled standard wet cell.

comprises of two 3” diameter, 5 mm thick coated silicon wafers as the working electrode and counter electrode. Both electrodes are fabricated by first growing a 100 Å thermal oxide on the silicon wafer to act as a barrier layer, then depositing a 150 Å tungsten film using the process described in Chapter 3. Lithium foil (Sigma-Aldrich) is smeared onto one of the wafers to act as the counter and reference electrode, and the other wafer becomes the working electrode. The two electrodes are electrically separated by a 500 μm thick Kalrez gasket, which is chemically compatible with the electrolyte. Electrolyte is inserted into a 1.5” diameter hole cut out of the center of the gasket, creating an electrochemically active area isolated from the atmosphere. The electrodes are clamped together between two thick silicon backing wafers for mechanical support.

Aluminum foil strips are placed between each electrode and the gasket to provide electrical access to the electrodes. While not used in this study, tubing through the side of the cell allows for electrolytes with different composition to be swapped in without disassembling the

cell. This cell is assembled in a helium-filled glovebox to prevent any oxygen or moisture from contacting either the electrode surfaces or the electrolyte.

The electrolyte used in this experiment is a 1 M LiPF_6 (BASF, >99%) salt in a 1:1 (v/v) mixture of EC (BASF, >99%) and DEC (CDN Isotopes, >99%). Deuterated solvents have significantly higher SLD than protonated solvents, which creates better contrast with the SEI (which is expected to have a relatively low SLD, given the high lithium content) and therefore lends higher sensitivity to the SEI in our study. Furthermore, because a majority of the SEI contents are expected to be formed from EC degradation products, rather than DEC degradation products, deuterating the DEC but leaving the EC protonated further enhances this contrast (deuterating the EC would increase the deuterium content of the SEI, thereby increasing its SLD). Trace water was removed from the EC before mixing by adding 3A molecular sieves (Sigma-Aldrich) at 40 °C for two hours.

The cell was then scanned with NR to study the structure in electrolyte prior to CV cycles, with the intent of characterizing the W anode in electrolyte with no SEI. However, it was found that a moderate short was present in the cell after construction, possibly due to small amounts of lithium detaching from the counter electrode and contacting the working electrode, or from intermittent contact of the Al foil leads. The open circuit voltage during scanning was near 500 mV as shown in Figure 4.3, much lower than the typical 1.4-1.5 V and well within the expected electrolyte reduction window. The OCV shows several spikes and further decreases by 120 mV over the course of ~20 hours, which may signal additional shorting events. In addition, as shown in Figure 4.4, the CV plots after NR data collection show considerable passivation even during the first cycle. Therefore, it is assumed that an SEI was grown prior to cycling. While NR data was collected over the entire 20 hour range, only data collected between hours ~2-5, where the

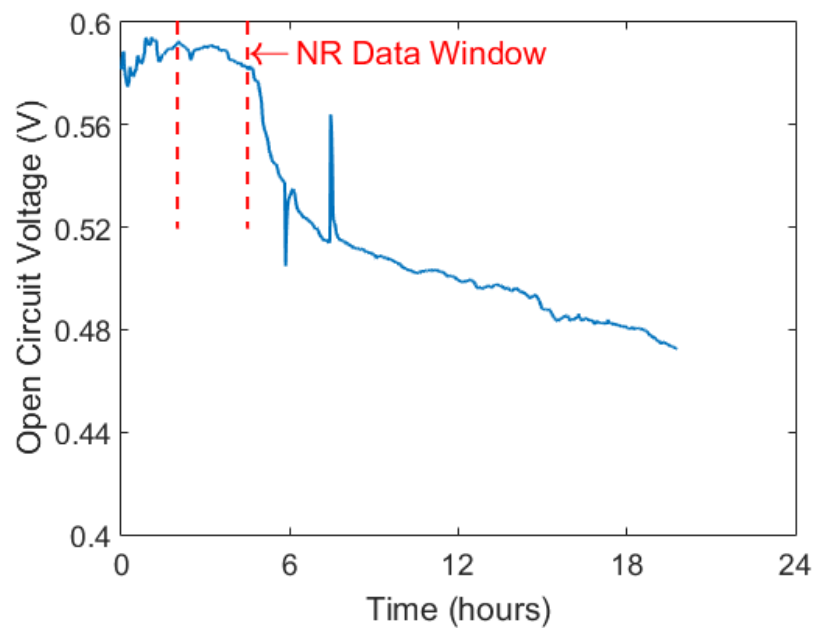


Figure 4.3: OCV during NR measurement of the working electrode in a wet cell.

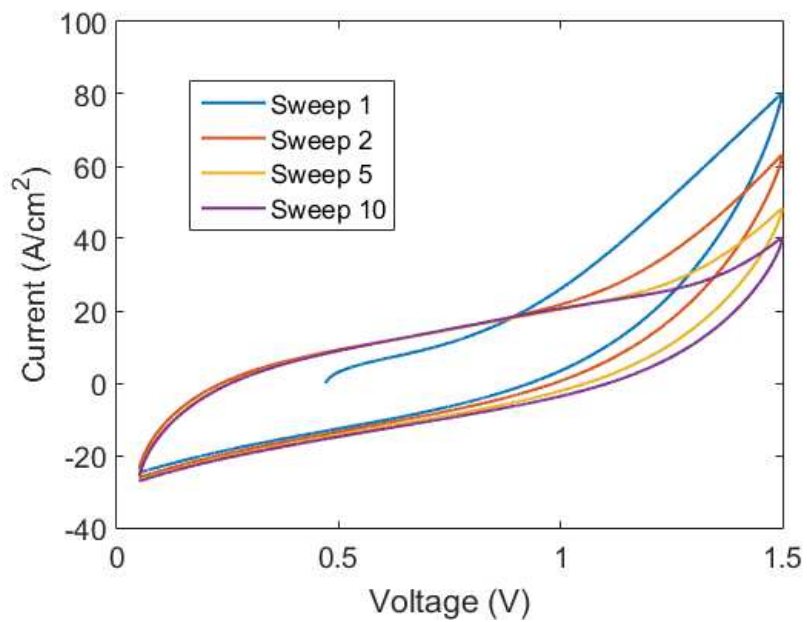


Figure 4.4: CV Sweeps after NR measurement

OCV was relatively stable, were analyzed for this study. This data set is henceforth referred to as ‘W1_ocv’ (i.e. tungsten sample #1, measured at OCV).

4.1.6 NR Measurement of the Non-Electrochemical Wet Cell

To confirm that any layered structures observed in W1_ocv are the result of electrochemical activity and not spontaneous chemical reactions between the electrolyte and working electrode, a second wet cell (sample W2) was assembled with no lithium on either electrode. The electrodes were fabricated with the same process as the first cell described in Chapter 4.1.4-4.1.5. As no lithium is present to function as a counter electrode, there is no possibility of shorting or electrochemical reactions. This NR data set is hereafter labeled ‘W2_electrolyte’ (tungsten sample #2, measured in electrolyte). Comparing the fitted SLD profiles for the W1_ocv and W2_electrolyte data sets will therefore help discriminate between layers formed due to spontaneous chemical reactions (W2_electrolyte) and those formed due to electrochemistry (W1_ocv).

4.1.7 NR Data Fitting

All NR data is fitted using the Refl1d software described in section 2.1.4. In this process, a model is proposed as a layered structure with three parameters: SLD, thickness, and interfacial width with the adjacent layer (i.e., roughness). The model is formulated within a python script file, where the user specifies the layers in the model, and can use mathematical expressions to relate layer parameters to one another (relating thickness and SLD for element conservation, for example), or to constrain the ranges of the fitting parameters in.

The substrate fabricated for this study consists of bulk Si (SLD fixed at its bulk value of $2.074 \cdot 10^{-6} \text{ \AA}^{-1}$, thickness = ∞), a thermally-grown SiO₂ layer (nominal SLD of $3.467 \cdot 10^{-6} \text{ \AA}^{-1}$, expected thickness = 100 Å), and a W layer (nominal SLD of $2.998 \cdot 10^{-6} \text{ \AA}^{-1}$, expected thickness

= 150 Å). These starting guesses are used to formulate models for the three data sets fitted as part of this work – W1_bare, W1_ocv, and W2_electrolyte. For all fits, the SLD and thickness of the SiO₂ and W layers are allowed to vary by roughly 15% to account for porosity and uncertainty in deposition, and the roughness is allowed to vary freely. The electrolyte acts as a bulk reservoir (nominal SLD of $3.77 \cdot 10^{-6} \text{ \AA}^{-1}$, thickness = ∞); given its known chemistry, the SLD of the electrolyte reservoir was fitted within a narrow window of its nominal value. Finally, the models also include three experimental parameters: theta offset (to account for slight misalignments between the sample and the neutron beam), background, and beam intensity.

To determine the nature of the SEI grown on tungsten, numerous models were used to fit the three data sets by proposing a range of interfacial layers in between the substrate and electrolyte. The model fit to W1_bare includes a surface layer to account for any potential oxides or trace contamination; the SLD, thickness, and roughness of this layer are given a wide range, given the uncertain chemistry of this layer. Three separate models for W1_ocv and W2_electrolyte are proposed, which include zero, one, and two surface layers, respectively, to represent SEI layers or layers formed through reactions between the substrate and electrolyte. As with the bare model, the SLD, thickness, and roughness of these layers are allowed to vary within a wide range.

Because the substrate layers (bulk Si, thermal SiO₂, and W) are expected to vary insignificantly during experiments on a given sample, the data sets W1_bare and W1_ocv were fit simultaneously and constraints were written into the python model file such that the Si and SiO₂ layer parameters match exactly in the models fit to the two data sets. The W SLD is allowed to vary between the two fits, but as any differences are expected to be from pores in this layer filling with either electrolyte or SEI compounds, the allowed deviation in W1_ocv from

W1_bare is made proportional to the fitted W porosity in W1_bare. Fitting the data in this manner eliminates extraneous fitting parameters (i.e. the simultaneous fit has six fewer parameters than fitting the two data sets independently), with a seventh parameter (the tungsten SLD fitted to W1_ocv) that has a very narrow range of possible value. By restricting the parameter space in this manner, Refl1d is more reliably able to locate the global minimum in χ^2 . Perhaps more importantly, the resulting fit locates a *single* model for the common substrate that is able to fit both data sets, which places greater confidence that the fitted model accurately represents the substrate structure and therefore places a greater focus on the fitting of the layers at the substrate/electrolyte interface. The python scripts used to generate the fits presented in this study are given in 6.2A.1 and 6.2A.2.

For each model, a DREAM fit with a large, uniformly distributed population is first performed to explore the entire parameter space. Once this fit has converged, it is used as an initial guess for a quick follow-up fit using a Nelder-Mead simplex algorithm to ensure the minimum in the well has been found. Finally, the results of this fit are used as a starting point for a second, shorter DREAM fit with a tightly packed initial population to obtain accurate uncertainty information for each parameter.

4.2 Results

This section presents the results of the EQCM-D and NR studies as well as preliminary analysis. More detailed analyses combining the results are given in the following chapter.

4.3 EQCM-D Experimental Results

Figure 4.5 shows the EQCM-D data (CV and mass uptake) during 10 CV sweeps between 0.05 and 1.5 V (vs. Li/Li+). During the first sweep, reduction peaks are observable at 800 mV and 275 mV, and a single oxidation peak at 1.0 V. The CV shape is very similar to that

measured on a Cu anode in a previous study [45], and is evidence that SEI formation is primarily a function of the electrode potential, and that measurement of the SEI on a non-intercalating electrode, as in this study, serves as a suitable first approximation of that grown on relevant Li-storage anode materials such as graphite and silicon. The subtle peak at 800 mV is attributed to reduction of electrolyte solvents, which is expected to begin at approximately at 1.2 V and continue for the remainder of the cathodic sweep. The large increase in current magnitude below 0.5 V corresponds to additional SEI formation, while the reduction peak at 275 mV is likely due to underpotential deposition (UPD) of lithium. Underpotential deposition occurs when the bonding interaction between a metal and a substrate is stronger than the bonding of the metal to itself. This phenomenon is attributed to the difference in work functions for the metals [60]. The oxidation peak near 1.0 V corresponds to the stripping of the Li UPD layer. The passivating effect of the SEI is clearly observed by the reduced current and mass deposition after each cycle. As shown in Figure 4.5(b), the net mass change is drastically reduced by the fifth sweep, with a net mass change of nearly zero in the tenth sweep. The decrease in mass during each oxidation sweep is attributed both to the stripping of the Li UPD layer and partial dissolution of the reduction products into the electrolyte, which corroborate the findings in the previous study [45].

By comparing Figure 4.5 (a) and (b), one can qualitatively see that the mass variations are passivated more effectively than the current. By cycle 10, there is no net mass gain per cycle, while significant reduction current is still observed in the 10th CV cycle in Figure 4.5(b). In a qualitative sense, this is important in that it implies imperfect passivation of the electrode by the SEI, and also that not all current delivered to the electrode is associated with a mass increase. This phenomenon will be quantified in Chapter 5, via m.p.e. analysis, and correlated with the NR results for a holistic picture of the SEI formation chemistry.

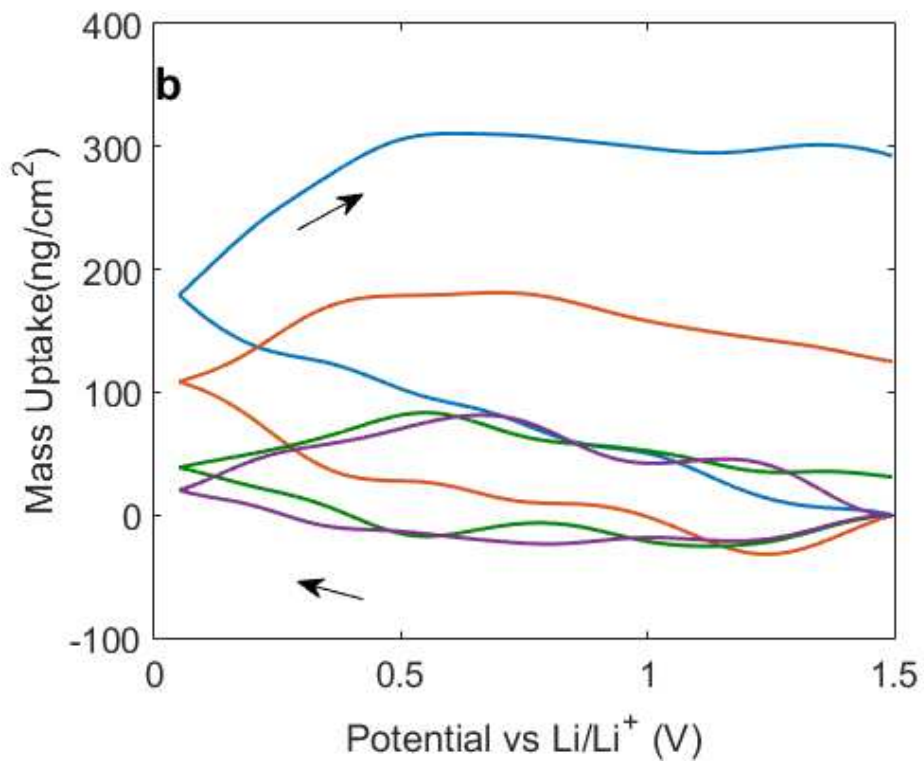
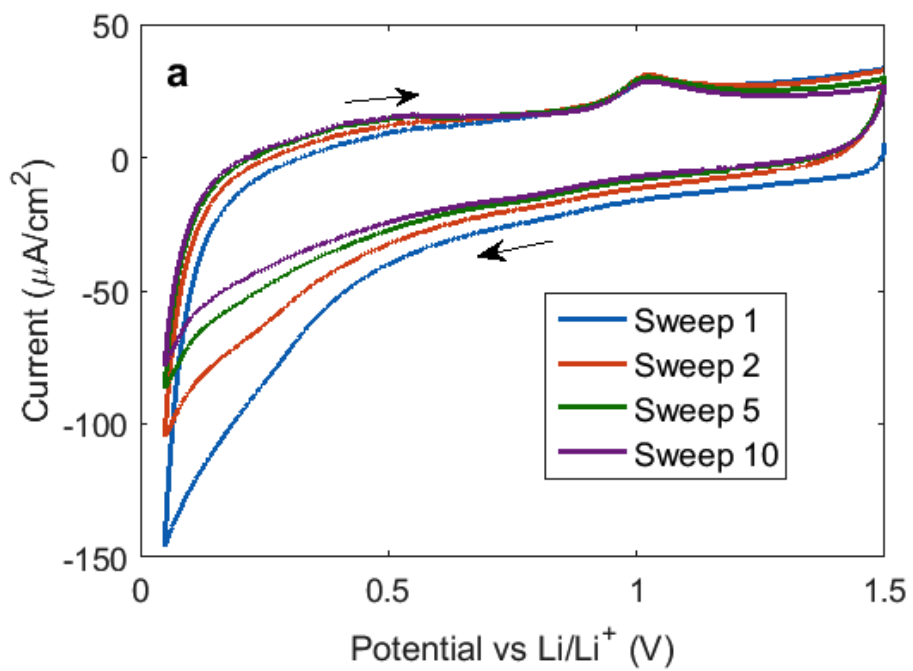


Figure 4.5: Plots of current and mass change on a fresh tungsten electrode during CV between 0.05 V and 1.5 V vs. Li/Li^+ . (a) Current; (b) Mass

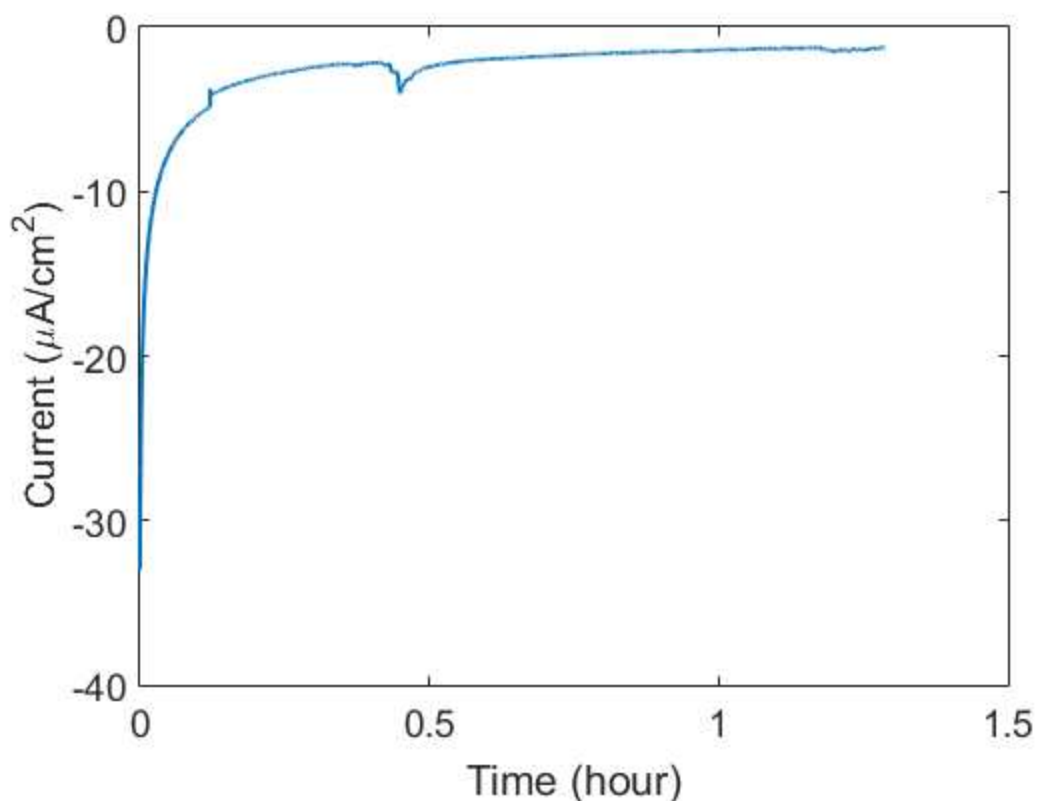


Figure 4.6: Current decay in EQCM cell following SEI growth at an electric potential of 250 mV (vs. Li/Li+), following the 10 CV cycles in Figure 4.2

Because NR is a relatively slow (~hours) measurement, it requires layered structures that are stable and unchanging over the course of the measurement. Because the SEI can partially dissolve at open-circuit voltage (OCV), NR of the freshly-grown SEI will be measured during a potentiostatic hold at 250 mV (vs. the Li/Li+ counter/reference electrode) after completion of the CV. To predict the amount of time required for the SEI electrochemistry to fully stabilize after growth during this hold, the experiment was simulated in our lab and the current in the EQCM cell was monitored. As shown in Figure 4.6, the current equilibrates to a small but negative value within approximately one hour after the potential hold begins. The current is not expected to fully decay to zero, as a small amount of leakage current is unavoidably present due to the finite electronic resistance of the electrolyte.

4.3.1 NR Experimental Results

Figure 4.7 through Figure 4.9 show (a) the collected and reduced NR data and (b) the best-fit SLD profiles for the NR data for conditions ‘W1_bare,’ ‘W1_ocv,’ and ‘W2_electrolyte,’ respectively. Layer parameters for each fit are given in Table 4.1, Table 4.2, and Table 4.4.

4.3.1.1 Substrate Layer (Si, SiO₂, and W) Parameters

In order to better determine the SLD profile of the substrate layers for sample W1, the NR data for W1_bare and W1_ocv were fit simultaneously in Refl1d, with constraints written into the fitting file to enforce near equality of the thicknesses and SLDs of all substrate layers, including the Si substrate, thermal silicon oxide layer(s), and tungsten anode (some small variations, on the order to 10%, were allowed). Due to slight porosity in the tungsten layer, the SLD of the tungsten layer is allowed to vary within a certain range to account for possible filling of pores with electrolyte, lithium, or SEI compounds. The density of the silicon substrate is expected to be very near the bulk value and the Si SLD is therefore held fixed at this value ($2.07 \times 10^{-6} \text{ \AA}^{-1}$) for all fits, to minimize the number of fitting parameters. The reported χ^2 value represents a goodness-of-fit parameter, with $\chi^2=1$ representing an ideal fit. Because of the statistical nature of NR, it is not always possible to achieve a perfect fit. As seen in Figure 4.7 and Figure 4.8, a suitable simultaneous fit to data sets W1_bare and W1_ocv required models with a two-layer structure for the thermally-grown silicon oxide. This substrate structure also improved the fits to the W2_electrolyte data, as seen in Figure 4.9 ($\chi^2 = 1.54$ without, $\chi^2 = 1.33$ with), and is also consistent with fits to X-ray reflectometry (XRR) data taken on a witness sample deposited simultaneously with the working electrode W1. It has been observed that thermally grown silicon oxides are slightly denser than bulk crystalline silicon, which is in line with the fitted parameter for the ‘outer’ SiO₂ layer (104%). The denser ‘inner’ SiO₂ layer,

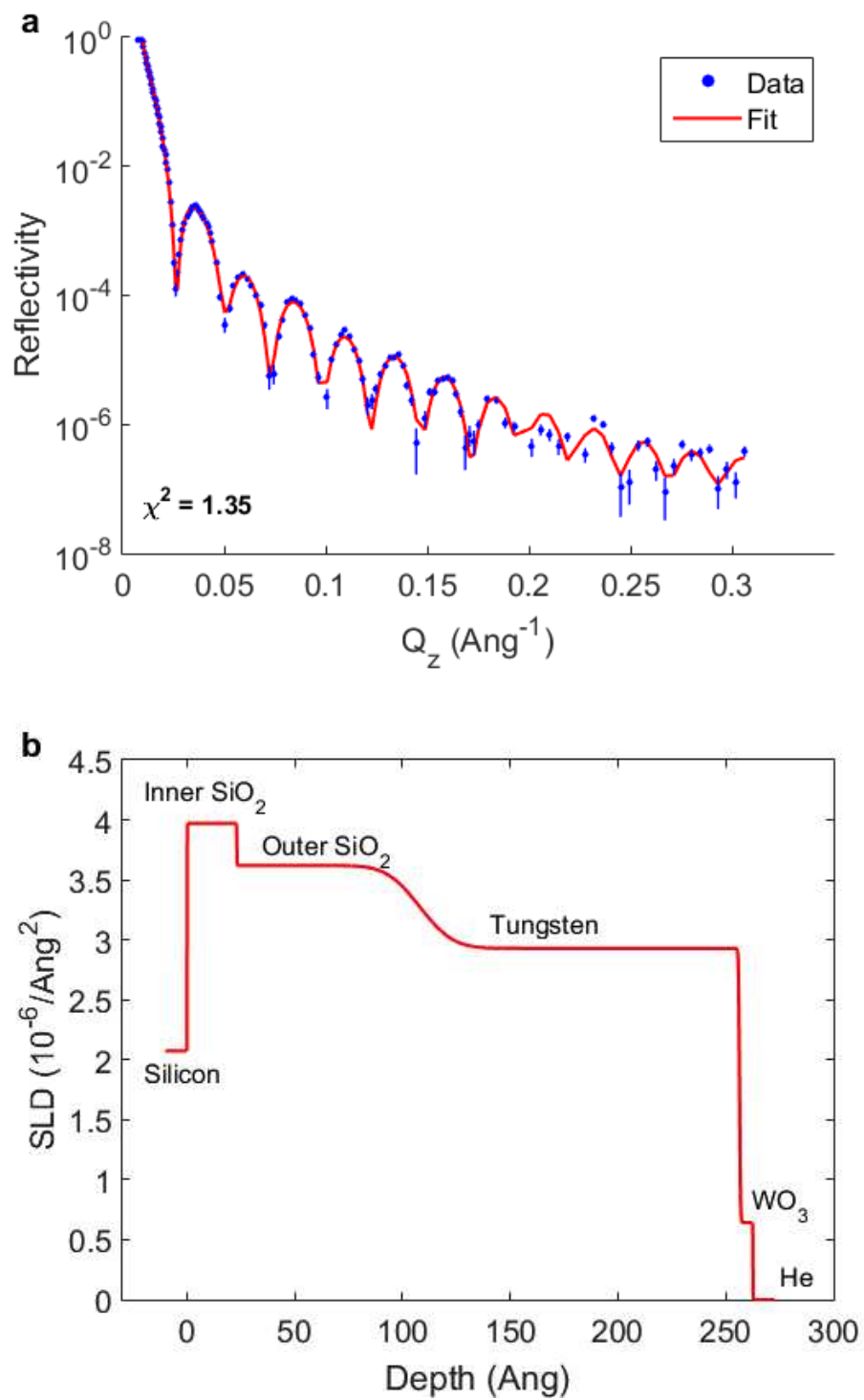


Figure 4.7: NR results for the bare working electrode in helium. (a) Reflectivity Data; (b) Fitted Profile

Table 4.1: Fitted parameters for bare working electrode in helium

Layer	Thickness (Å)	Density (% of bulk)
Inner Silicon Oxide (SiO ₂)	23.1	114%
Outer Silicon Oxide (SiO ₂)	84.9	104%
Tungsten	148.4	98%
Tungsten Oxide (WO ₃)	6.2	16%

meanwhile, may result from oxidation or thermal decomposition of trace contaminants on the silicon wafer during the thermal oxide growth process. It is also possible that this ‘inner’ SiO₂ layer is a fitting artifact that does not represent the physical structure of the substrate (“symmetry-type” operations where two layers switch positions can often give rise to similar NR spectra). However, the fact that the bilayer SiO₂ structure improves the fits or is consistent with fits to three separate samples (W1, W2, and the witness sample) and in two separate chemical environments (vapor and electrolyte) provides strong evidence that the profile in Figures 4.7 through 4.9 accurately represents the structure of the thermally-grown SiO₂.

Finally, as shown in Figure 4.7 through Figure 4.9 and reported in Table 4.1, Table 4.2, and Table 4.4, the thickness of the tungsten layer and added thicknesses of the silicon oxide layers closely match the target values, and agree well with auxiliary XRR measurements on the sacrificial witness sample. The tungsten layer density is found to be close to bulk value. Due to limitations in the sputter deposition process, it was not possible to completely prevent exposure of the tungsten film to atmosphere, and fitting reveals a thin surface layer. This is modeled as a porous tungsten tri-oxide (WO₃, bulk SLD = $4.1 \times 10^{-6} / \text{Å}^{-2}$), but the thickness (6.2 Å, below the resolution limit of the NR technique) and low SLD could mean that the layer is formed by trace atmospheric contaminants, is some other tungsten oxide, or may even simply be an alternative representation of surface roughness at the interface between the tungsten and the vapor.

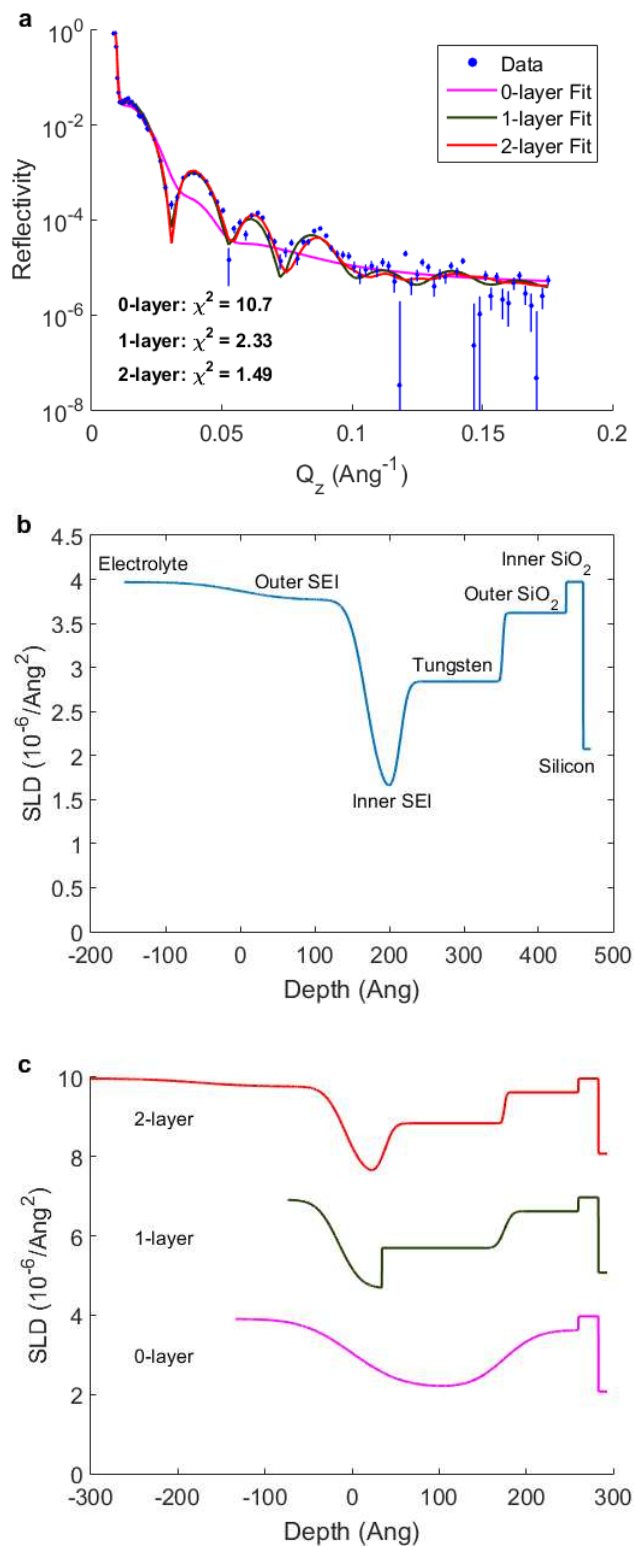


Figure 4.8: NR results for the working electrode after SEI growth, for 0, 1, and 2 surface layer models. (a) Reflectivity data; (b) Fitted profile for 2-layer model; (c) Comparison of fitted profiles of all models

Table 4.2: Fitted parameters for 2-layer model on working electrode after SEI growth

Layer	Thickness (Å)	Thickness 95% CI	SLD ($10^{-6}/\text{Å}^2$)	SLD 95% CI
Tungsten	134.8	[132.1, 140.2]	2.77 (92% bulk)	[2.42, 2.87]
Inner SEI	48.7	[41.4, 53.7]	1.66	[1.46, 1.88]
Outer SEI	207.8	[152.9, 214.9]	3.71	[3.61, 3.73]
Electrolyte	-	-	3.913	[3.911, 3.915]

Table 4.3: Calculated BIC for W1_ocv models

Model	χ^2	BIC
0-layer	10.7	355.6
1-layer	2.33	179.9
2-layer	1.49	142.4

4.3.1.2 Analysis of the Electrode-Electrolyte Interface – Identification of the SEI

As mentioned in section 4.1.5, the low OCV (~500 mV) after cell assembly supports the idea of an unintended short between the working and counter electrodes. This is further supported by the CV scans taken immediately after cell assembly (Figure 4.3), which show high levels of passivation and very little current density beyond simple double-layer charging (this in contrast to the significant reduction current seen below ~800 mV in Figure 4.5). The oxidation current seen > 1.0 V in Figure 4.3 is likely due to trace contaminants or gaseous products that formed due to the shorting of the battery. The latter is perhaps more likely, given the use of the molecular sieves prior to cell assembly to purify the electrolyte solvents.

Regardless of the low OCV's cause, it is evident that the anode immediately sat at voltages well below the SEI formation threshold, making it highly likely that an SEI did grow.

To explore the nature of the any SEI grown after battery assembly, simultaneous fits to W1_bare and W1_ocv employed three separate models, which allowed either zero, one, or two distinct layers at the tungsten-electrolyte interface. The calculated reflectivities for the 0-layer, 1-layer, and 2-layer fits are given in Figure 4.8 (a). While the 1-layer and 2-layer models both give acceptable χ^2 values, the BIC calculation in Table 4.3 shows a difference of 37 between the two models, revealing a very clear preference for the 2-layer model. The corresponding 2-layer SLD profile that is fit to the resulting NR data (Figure 4.8 (b) and Table 4.2) reveals that a dual-layer SEI-like film was indeed formed, similar to findings in literature [25]–[31]. The outer SEI is fairly thick (~ 208 Å) and has an SLD quite close to that of the electrolyte, which suggests it is porous and composed of higher-SLD organic compounds such as $(\text{CH}_2\text{OCO}_2\text{Li})_2$ and its deuterated equivalent ($2.95 \cdot 10^{-6}/\text{Å}^2$ and $5.84 \cdot 10^{-6}/\text{Å}^2$, respectively). On the other hand, the inner layer is similar to that observed by Owejan, et al. [45], with a similar thickness (48.7 Å) and has relatively low SLD, suggesting it lacks high-SLD reduction components and is rather composed of lower-SLD inorganic compounds such as LiOH ($0.06 \cdot 10^{-6}/\text{Å}^2$), Li_2O ($0.812 \cdot 10^{-6}/\text{Å}^2$), and LiF ($2.301 \cdot 10^{-6}/\text{Å}^2$). The high contrast in SLD between the electrolyte and this layer suggest that it is fairly dense. Again, quantitative analysis will be undertaken in Chapter 5, but even a qualitative scan of the SEI's SLD profile shows the benefit of the improvements made for enhanced sensitivity, as this study is able to resolve the previously unobserved “outer” SEI layer. Due to the uncertain nature of the SEI formation on sample W1, an additional NR measurement was made on sample W2 in contact with electrolyte, but with no counter electrode (and therefore no possibility of an electrochemical reaction). The goal of this measurement (‘W2_electrolyte’) was to diagnose whether or not the interfacial structure in Figure 4.8 could have been formed by non-electrochemical means (i.e., whether or not it is truly an SEI). The fitted SLD profile is

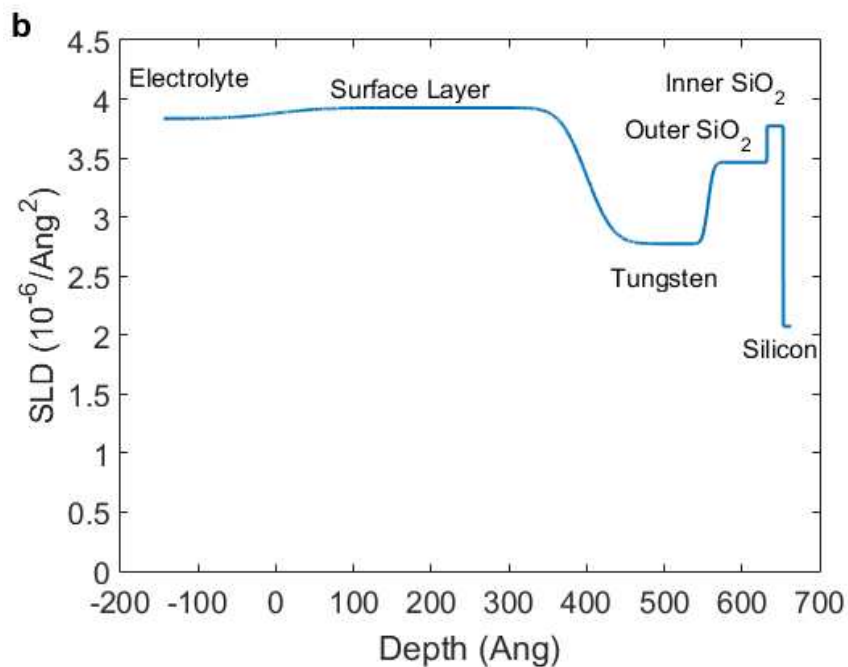
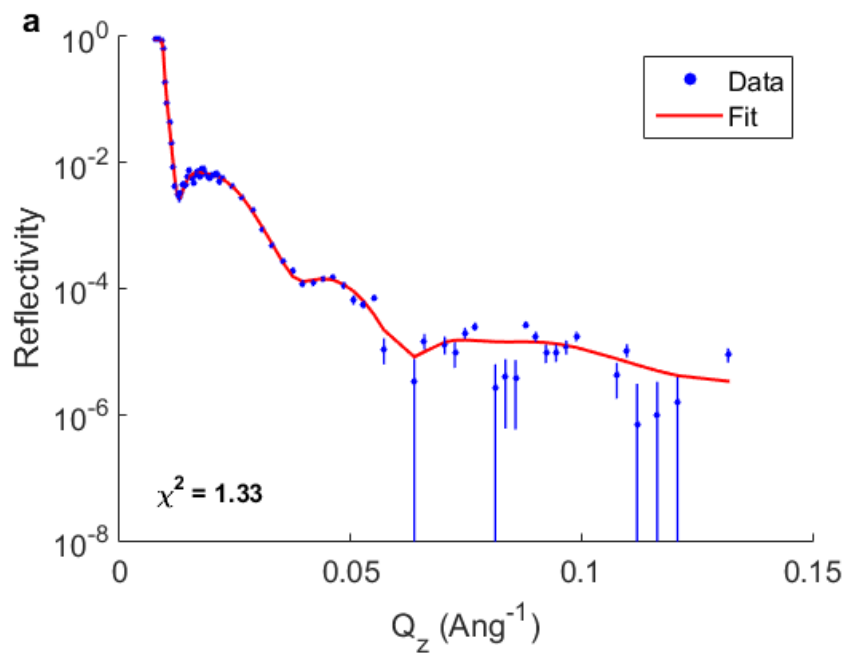


Figure 4.9: NR results for a working electrode in electrolyte with no lithium counter electrode. (a) Reflectivity Data; (b) Fitted Profile

Table 4.4: Fitted parameters for working electrode in electrolyte with no counter electrode

Layer	Thickness (Å)	SLD ($10^{-6}/\text{Å}^2$)
Tungsten	156.5	2.77 (92% bulk)
Surface Layer	400.0	3.95
Electrolyte	-	3.83 (101% bulk)

given in Figure 4.9, and the best-fit layer parameters in Table 4.4. A thick surface layer appears to be present with an SLD slightly higher than that of the electrolyte, which has been reported in previous studies [45], [50] and attributed to a carbonate/hydroxide liganding layer. The thin, low-SLD layer in Figure 4.8 is absent here, confirming that the layer in W1_ocv is formed from electrochemical activity and not surface reactions with the electrolyte. Including the dual-layer silicon oxide from fits to W1_bare and W1_ocv significantly improved the fit (relative to initial fits with a single-layer SiO₂), supporting the fits in Figure 4.7 and Figure 4.8 and suggesting that the structure is real rather than just a fitting artifact.

4.4 Conclusion

In this chapter, we have characterized an SEI grown on a tungsten anode using the deposition process detailed in Chapter 3 using EQCM-D and NR measurements. Despite an unanticipated short in the NR cell, the resulting SEI-like structure is confirmed to be the result of electrochemical activity, and both OCV data during NR data collection and CV cycles taken afterwards provide strong evidence that the structure is indeed an SEI. The fitted data shows a dual-layer structure to the SEI in accordance to previous computational and experimental studies in literature mentioned in Chapter 2. This marks this study as one of the first direct *in operando* measurements of a dual-layer SEI. With the NR and EQCM-D data, we can now begin to create a quantitative understanding of the chemical composition of the SEI.

CHAPTER 5

SEI FORMATION AND COMPOSITION ANALYSIS

The previous chapter presented experimental data from three in operando techniques: NR spectra (and the SLD profiles associated with their fitting), electrochemical data (CV scans and chronoamperometry), and QCM-D. In this chapter, we will demonstrate quantitative analysis of the combined suite of measurements for a holistic picture of the chemistry of SEI formation.

5.1 Mass Per Electron (m.p.e.) Analysis

In order to gain a clearer mechanistic understanding of the SEI growth process, the EQCM data shown in Figure 4.5 is used to calculate the m.p.e, as described in section 2.2.2:

$$m.p.e = F \frac{\Delta m}{\Delta Q} \quad (5.1)$$

Where F is Faraday's constant, Δm is the change in mass, and ΔQ is the corresponding change in charge (found by integrating the current density $I \times dt$ over the given time domain). Any reduction reactions that involve Li^+ ions will involve both charge and mass transfer to the anode surface, and will therefore contribute to the m.p.e. By counting the number of Li atoms in an expected SEI compound, the theoretical m.p.e for a given reduction product can be calculated. Table 5.1 lists several common SEI components and their theoretical m.p.e values.

Figure 5.1 shows calculated m.p.e values over the electrolyte reduction window for the first and second cycles. The primary EC reduction product is expected to be lithium ethylene dicarbonate (LEDC), which has an m.p.e of 81 g/mol e^- . The initial m.p.e near 1.2 V suggests the formation of this species, in addition to other heavier organic compounds of the form $(\text{ROCO}_2\text{Li})_2$. While the formation of LEDC is expected to continue over the whole reduction

Table 5.1: m.p.e values for common SEI components

Compound	m.p.e (g/mol)
Li	7
Li ₂ O	15
LiO ₂	19
LiOH	24
LiF	26
Li ₂ CO ₃	37
(CH ₂ OCO ₂ Li) ₂	81

sweep, we observe a significant drop in the m.p.e value as the anode electric potential decreases below 1.0 V. This reflects the precipitation of lighter inorganic compounds, which may form via several mechanisms. Trace water and oxygen in the electrolyte will reduce to form LiOH (24 g/mol e⁻), LiO₂ (19 g/mol e⁻), and Li₂O (15 g/mol e⁻). The LEDC and other organic compounds may also react with trace water and HF and dissolve back into the electrolyte, leaving behind Li₂CO₃ (37 g/mol e⁻) and LiF (26 g/mol e⁻). In addition, Li UPD (7 g/mol e⁻) at low potentials will further decrease the m.p.e.

Subsequent cycles are seen to follow a similar pattern of higher m.p.e near the beginning of the reduction sweep and progressively lower values over the course of the sweep, but with significantly lower m.p.e. magnitudes than during the first sweep. As the m.p.e only captures reactions with nonzero charge transfer, dissolution of SEI compounds into the electrolyte will contribute to a mass loss. This can lead to low or even negative m.p.e values once the SEI has stabilized.

Finally, while not shown in Figure 5.1, the m.p.e value for the oxidation peak near 1.0 V is calculated to be 5.1 g/mol e⁻. Combined with the lack of passivation during cycling, this peak is confirmed to be from the stripping of the Li UPD layer.

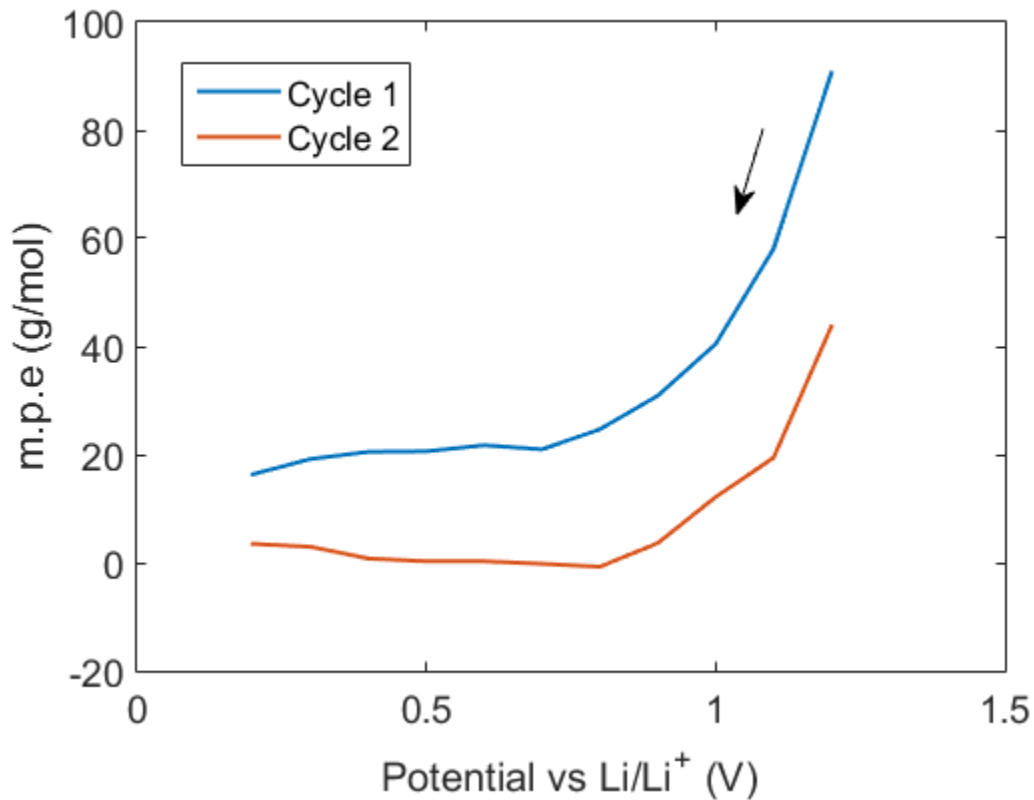


Figure 5.1: m.p.e values calculated over the reduction sweep for the 1st and 2nd cycles

5.2 Composition Analysis by Monte Carlo Simulation

While multiple previous NR studies have observed the SEI on a range of substrates [46], [48]–[50] quantitative analysis of the SEI composition has proven difficult, for a number of reasons, including poor NR contrast for the SEI (as in Owejan et al. [45]), noisy data/questionable fits which are not of sufficient quality (i.e. high χ^2 values) to support detailed quantification of the observed SEI, and a general lack of complementary *in operando* data to help constrain the system of equations needed to specify the SEI composition.

However, the current study appears to have addressed each of the aforementioned obstacles – via improved SLD contrast between the SEI and adjacent layers, high quality NR fits ($\chi^2 = 1.49$ is the worst of the three fits presented), and complementary EQCM-D data taken in parallel under similar experimental conditions – such that quantification of the SEI composition now appears feasible. In this chapter, we combine the EQCM-D mass uptake measurements with the SLD profile from the NR data to obtain a detailed understanding of the SEI formation chemistry. In particular, we describe and apply a Markov-Chain Monte Carlo based composition fitting tool developed as part of this study, which leverages the Bayesian approach to NR fitting in the Refl1d software for quantitative predictions of the chemical composition of the SEI, given the mass, thickness, and SLD data presented in Chapter 4. The modeling tool developed generates a large number of possible SEI physical models and filters them using (a) the total mass from QCM, and the probability distributions the SEI (b) layer thickness and (c) SLD values from NR to generate a statistical model of the most likely composition.

The candidate SEI components are identified based on previous literature [29], [33], [34], [45]. The inner SEI is expected to be primarily composed of inorganic compounds, and is therefore proposed to contain four components: Li_2O , LiOH , Li_2CO_3 , and LiF . Because LiOH is expected to form primarily from the reduction of water, its deuterated equivalent is not considered. The outer SEI is expected to be composed of organic compounds, and is proposed to contain LEDC and deuterated LEC, the primary reduction components of EC and deuterated DEC, respectively. The ratio of LEDC to deuterated LEC will therefore give us an estimate of the ratio of EC decomposition to DEC decomposition. In addition to the SEI components, the porosity of each layer is calculated by considering electrolyte as one of the constituents of each SEI layer.

To generate SEI composition candidates, a maximum thickness for each layer in the SEI is first chosen based on the probability distribution of the fitted SEI layer thicknesses from the NR study in section 4.3.1. The SEI composition fitting routine next generates a random vector of “partial thicknesses,” $t_{k,i}$, one for each SEI component k in each of the two layers i , where $t_{k,i}$ is allowed to vary between 0.0 and the maximum thickness chosen for that layer. The proposed total layer thickness for each layer i (inner SEI or outer SEI), $t_{total,i}$ is thus calculated by summing over the partial thicknesses in that layer, and volume fractions $V_{k,i}$ for each SEI component are calculated by dividing its partial thickness by the total layer thickness:

$$t_{total,i} = \sum_k t_{k,i} \quad (5.2)$$

$$V_{k,i} = \frac{t_{k,i}}{t_{total,i}} \quad (5.3)$$

This, in turn, enables calculation of the layer SLD via equation 2.5, based on the volume fractions $V_{k,i}$ of each constituent phase. The SEI areal mass, m_{SEI} (ng/cm²) can also be calculated by summing the product of the partial thicknesses times the density of the constituent material, summed over both the inner and outer SEI layer:

$$m_{SEI} = \sum_i \sum_k t_{k,i} \rho_{k,i} \quad (5.4)$$

Having calculated the layer thicknesses, SLDs, and total SEI mass for the proposed array of partial thicknesses, the proposed composition is either accepted or rejected, based on how well it agrees with the corresponding EQCM-D and NR data. First, the composition is rejected

outright if the total SEI areal mass is not within $\pm 20\%$ of that from the EQCM-D measurements. For physical models which are not rejected, the posterior distributions from Ref11D for the inner and outer SEI thickness and SLD values are used as an approximation of the probability distribution to calculate a mean and standard deviation for each parameter (assuming a normal distribution). These parameters, in turn, are used to calculate the probability that the SLD and thickness values (one each for the “inner” and “outer” SEI layers) for the proposed physical model come from the same distributions as the NR data. These four values are subsequently averaged to calculate p , the average probability that the proposed physical model represents the SEI grown on sample W1, given the NR data. Finally, the Metropolis algorithm is employed to accept only compositions with a high probability of being observed, given the prior assumptions regarding the NR fitting results. A random number N between 0 and 1 is generated, and the composition is ultimately “accepted” if $p \geq N$. At this point, “accepted” SEI models are stored in a matrix for post-processing, rejected models are discarded, and a new random array of partial thicknesses is generated and analyzed. This process is repeated until 20,000 total compositions have been accepted. Histograms showing the population distribution of the volume fractions of each component for the inner and outer layers are shown in Figure 5.2 and Figure 5.3, respectively. The mean values for each component volume fraction in each layer are reported in Table 5.2 and Table 5.3. While there is still a great deal of uncertainty in the presented histograms (volume fractions generally span a range $\sim 50\%$ for each component), the mean values of the volume fractions for each layer sum to 1 (which is a result of the fitting, i.e. it was not externally imposed as a constraint), and represent the most likely composition. The relatively high amount of LiOH in the inner layer matches the previous study [45], and indicates trace moisture in the electrolyte as LiOH is the result of both direct reduction of water and reactions of

Table 5.2: Inner SEI Mean Component Volume Fractions

Component	Mean Volume Fraction
Li ₂ O	0.246
LiF	0.199
LiOH	0.271
Li ₂ CO ₃	0.155
Electrolyte	0.123

Table 5.3: Outer SEI Mean Component Volume Fractions

Component	Mean Volume Fraction
LEDC	0.514
Deuterated LEC	0.057
Electrolyte	0.428

Li₂CO₃ with water. A high amount of Li₂O is also expected since it is the primary reduction compound of oxygen as well as a possible reduction compound of water. The porosity (12.3%, calculated as the volume fraction of electrolyte) is fairly low, which reflects the high contrast between the inner SEI SLD and electrolyte SLD in the NR data, and also supports the view that the inner SEI is a dense layer.

In contrast, the outer SEI is found to be highly porous, which again agrees with the low SLD contrast between this layer and the electrolyte in the NR data. The mean volume fraction of deuterated LEC is only a tenth that of LEDC, which confirms the conventional wisdom that the SEI is formed primarily from EC products. Simulations that allowed inorganic compounds in this layer returned very few acceptable compositions, all of which had extremely low volume fractions for these compounds, so it is unlikely that any significant amount of inorganic compounds exists in the outer layer.

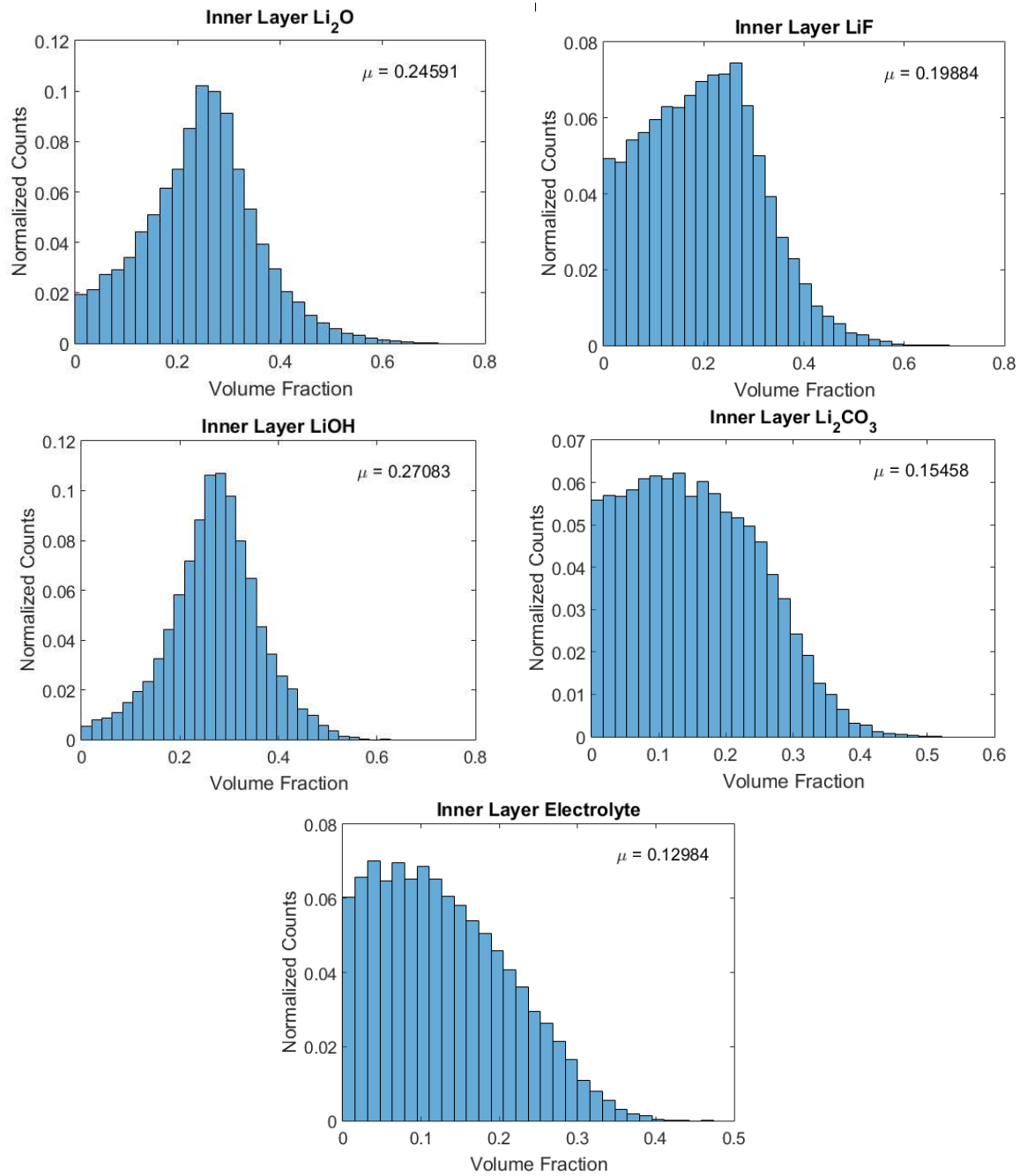


Figure 5.2: Histograms of inner SEI component volume fractions

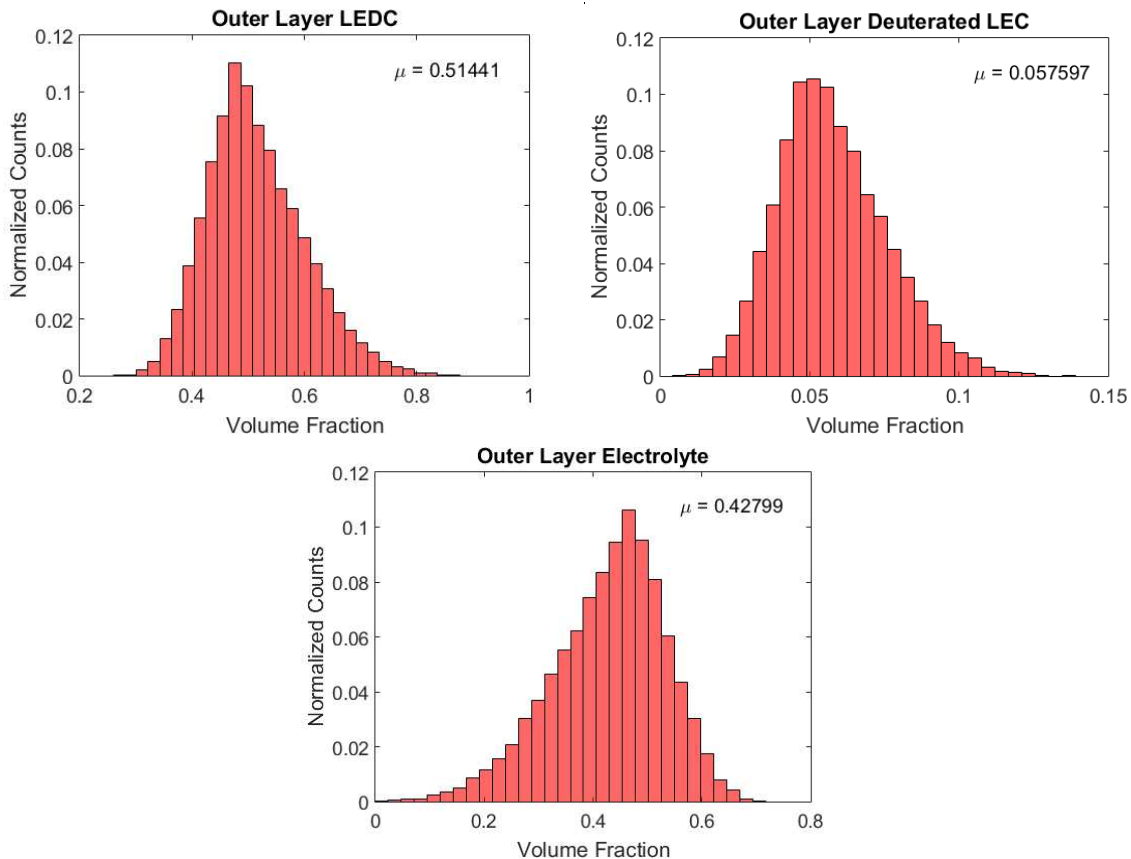
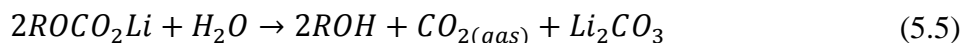
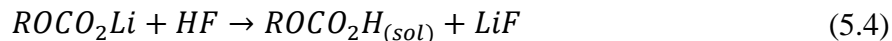


Figure 5.3: Histograms of outer SEI component volume fractions

For further quantitative insight, the m.p.e for the composition and thickness of the most likely SEI (from Table 5.2 and Table 5.3), is calculated to be 65.5 g/mol e^- . In contrast, the total calculated m.p.e for the EQCM-D experiment in section 4.3 is only 17.6 g/mol e^- , barely a quarter of what is measured by NR. This implies that significantly more charge has gone into forming the SEI in the EQCM and NR experiments than should theoretically be needed. Again, this can be deduced by comparing the mass uptake and CV scans in Figure 4.5, which show no net mass uptake by cycle 10, but a net reducing current. This was observed previously via NR [45], and is primarily due to dissolution of SEI compounds, as has been discussed. The wide difference in theoretical vs observed m.p.e suggests that high m.p.e compounds such as LEDC

and other organic compounds are dissolved, non-electrochemically, by the electrolyte. This is supported by the presence of LiF and Li₂CO₃ in the inner SEI, which are both results of the decomposition of ROCO₂Li compounds. Aurbach gives possible mechanisms for this decomposition [37], [61]:



The decomposition of high m.p.e compounds to lower m.p.e compounds drives down the measured m.p.e, yielding the low value seen in the EQCM experiment.

5.3 Conclusion

In this chapter, we have combined the EQCM-D and NR measurements using m.p.e analysis and a Markov-Chain Monte Carlo fitting procedure developed in-house to build a holistic picture of the SEI composition and formation chemistry. The m.p.e analysis shows that electrolyte solvents reduce first to create heavy organic reduction products, particularly LEC and LEDC. However, the diminishing m.p.e values over each cycle suggests that these organic compounds are reacting with trace impurities in the electrolyte to form lighter, inorganic compounds like LiF, Li₂O, LiOH, and Li₂CO₃ that settle on the anode surface. This creates the dual-layer SEI structure seen in the NR data, with a thin, compact, rigid inner layer composed of inorganic compounds and a thicker, porous, softer outer layer of organic compounds. While the inner SEI forms by decomposition of the outer SEI, some portion of the remaining organic compound decomposition products dissolve back into the electrolyte, resulting in the total m.p.e

of the SEI being much lower than anticipated from the calculated SEI composition and physical structure seen in the NR data.

CHAPTER 6

FUTURE WORK AND CONCLUSION

This section details work that either represents current efforts or new potential channels for future research, as well as a summary of the work completed in this thesis and its implications for future research.

6.1 Future Work

While this study has succeeded in enhancing the sensitivity of NR measurements to the SEI, allowing for much higher resolution characterization, this project represents only a milestone in seeking an intimate understanding of the SEI. Listed below are several avenues for improvements or follow-up studies.

6.1.1 Improved NR Cell Design and High-Temperature Measurements

The original goal of this project was to be able to study the SEI evolution during a thermal spike in order to determine the exothermic chemistry that leads to thermal runaway in Li-ion batteries. However, it was found that the current setup for NR experiments is inadequate for elevated temperature measurements for two primary reasons:

1. The moderate shorting observed in section 4.3.1 is believed to be due to lithium flaking or detachment from the counter electrode, where it can then potentially create a bridge to the working electrode. Therefore, a better process of fabricating the counter electrode is needed. The approach used here involved smearing the lithium onto the counter electrode, but pressing it on instead with a stainless steel roller may decrease the chance of delamination. Alternatively, a lithium alloy can be created to act as the counter electrode, such as by

pressing Li to an aluminum substrate and heating. A follow-up NR study using the former approach has already been conducted, and data analysis is currently underway to determine the properties of the SEI grown in this setup.

2. LiPF_6 salts readily decompose at elevated temperatures to form gases and increase the cell pressure, which was found to push electrolyte out of the cell through the Kalrez gasket. Even at relatively moderate temperatures such as $80\text{ }^\circ\text{C}$, the cells were found to be mostly dry after disassembly. The formation of bubbles accompanied by a loss of electrolyte can quickly degrade NR data, as it not only forms a heterogeneous electrolyte layer, but the loss of ionic contact between the electrodes also causes non-uniform SEI growth across the anode surface. To be able to properly characterize a heated cell with NR, a wet cell with a much stronger seal is needed, which will likely require a complete redesign. This is especially true at higher temperatures exceeding the boiling point of DEC ($127\text{ }^\circ\text{C}$).

In addition to the NR experiments, EQCM experiments can be done at higher temperatures. This is currently not feasible as the open module is only rated to $60\text{ }^\circ\text{C}$, which is below the temperature at which the signature thermal decomposition reactions are expected to occur. A high-temperature chamber rated up to $150\text{ }^\circ\text{C}$ is available from Q-Sense, but would need to be procured and retrofitted to allow simultaneous electrochemical measurements.

6.1.2 SEI Characterization for Varying Electrolyte Composition

This study uses a “standard” LiPF_6 electrolyte that is used in commercial batteries, but there is currently significant research into the performance of other salts which promise an SEI with enhanced chemical and thermal stability. The SEI composition is highly dependent on the electrolyte, and an SEI grown with another electrolyte may exhibit significantly different structure than the SEI characterized in this study. Therefore, once the NR experimental

procedure has been refined to the point thermal studies can be made, the next logical step would be to compare the thermal performance of different electrolytes.

6.1.3 Refinement of the Monte Carlo Simulator

Currently, the SEI composition modeler uses the mean and 68% confidence intervals reported by NR fitting to model a normal probability distribution for relevant parameters. However, the true probability distributions of the parameters from the NR results are not necessarily normal. In addition, layers with high interfacial widths often have different effective SLD than the fitted SLD parameter. While the modeling tool is an effective method for calculating not only a “most likely composition” but also the true uncertainty in each volume fraction, the tool is only as accurate as its inputs, and directly being able to use the true probability distribution from the Refl1D output files would increase its utility. Refl1D is written entirely in open-source python scripts, and so this is certainly feasible, but requires development of the appropriate software routines.

6.1.4 Structural Study of the Thermal Oxide on the Working Electrode

The NR fitting in section 4.3.1 yielded a dual-layer structure to the silicon oxide, which appeared in all three reported fits. While this strongly suggests the structure is real and not just an artifact of the fitting process, the structure is unexpected and its actual identity and formation mechanism are not well understood. Follow-up characterization of this structure using other techniques such as SEM could shed light on this phenomenon.

6.1.5 NR Comparison of the Shorted Cell vs. a Cycled Cell

As mentioned above, a better process of counter electrode fabrication is needed to create a short-free cell that can be cycled as in the EQCM-D experiments. Analysis of an SEI grown in

such a cell is currently underway. However, in the case that SLD profile varies considerably between sample W1 and this follow-up study, the data taken of the SEI grown on the shorted cell is still quite valuable, as dendritic growth in actual batteries can lead to a similar internal short. SLD profiles can readily be compared between the shorted cell and the cycled cell to study how the SEI varies between the two cases, providing valuable insight into the properties of the SEI in shorted cells.

6.2 Conclusion

This study expands upon prior neutron reflectometry experiments on the SEI layer in lithium-ion batteries to improve sensitivity of the measurements to the SEI. Tungsten was determined to be a superior non-intercalating anode material for NR measurements due to the improved contrast it provides between the SEI and adjacent layers. It was found that sputter deposition of tungsten at 3 mTorr chamber argon pressure and 15 W sputtering power yielded tungsten thin films with the optimal characteristics for NR measurements. The properties of the tungsten films were confirmed using atomic force microscopy and x-ray reflectometry.

Electrochemical quartz crystal microbalance techniques were used to perform initial characterization of SEI films grown on tungsten anodes. The electrochemical behavior of the SEI on tungsten was found to be similar to one grown on a non-intercalating copper anode in a previous 2012 study [45], confirming that SEI reduction process vary rather weakly with the electrode material, and the SEI grown on an non-intercalating anode serves as a suitable first approximation for that grown on graphite or other technologically relevant anode materials. An m.p.e analysis on the EQCM data showed the reduction of expected SEI compounds, as well as both the passivating effect of the SEI and the partial dissolution of the SEI during cycling, as observed qualitatively in the 2012 study [45].

NR was then used to determine the depth profile of the SEI SLD (which is, in turn, related to its composition). The tungsten anode was first characterized in helium to confirm the substrate structure. The tungsten anode was then assembled into a wet cell, during which a moderate short was unintentionally introduced, immediately forming an SEI-like structure on the tungsten surface. NR data on a separate wet cell with no lithium counter electrode does not exhibit the structure present in the shorted cell, confirming that it is the result of electrochemical activity and not spontaneous chemical reactions at the electrode surface. Combined with low OCV and visible passivation in the CV curves, the evidence suggests that this structure is an SEI layer. Fitting of the NR data on the shorted cell reveals a dual-layer structure to the SEI, with a thin, low-SLD inner SEI and a thick, high-SLD outer SEI. While this structure has been suggested by numerous simulations, destructive *ex situ* depth profiles, and viscoelastic modeling of QCM-D data, this study represents one of the first direct *in operando* observations of the two-layer SEI structure. This was made possible by the enhanced sensitivity of the tungsten anode, as the outer SEI layer shows only weak contrast with the electrolyte.

Finally, the EQCM and NR data were combined to build a quantitative understanding of the SEI composition on tungsten. A Markov Chain Monte Carlo simulation was created to generate a large pool of possible SEI compositions based on the parameters of the NR fit and the mass measurements from the QCM data. This confirmed that the inner SEI is a dense layer composed mainly of light inorganic compounds: roughly 25% Li_2O , 20% LiF , 27% LiOH , 15.5% Li_2CO_3 , and 12.5% electrolyte (porosity). On the other hand, the outer SEI is a porous layer composed mainly of heavier organic compounds: roughly 51% LEDC (EC reduction products), 6% LEC (DEC reduction products), and 43% electrolyte (porosity). The SEI from the NR data is found to be much lighter than the charge measurements in the EQCM-D experiment

would suggest, supporting the proposal that the SEI partially dissolves during cycling. The low total m.p.e of the EQCM experiment combined with the presence of LiF and Li₂CO₃ in the inner layer suggests that organic reduction compounds react with trace impurities in the electrolyte to form the passivating inner layer, while simultaneously releasing mass into the electrolyte as dissolved products. This study represents a first step to leverage the powerful capabilities of NR as *in operando* probe of basic SEI chemistry for quantitative analysis of the SEI composition. The results lend new specific, quantitative rigor for the analysis of SEI formation and evolution mechanisms, and lay the groundwork for a promising array of follow-on studies on the development of stable and low-impedance SEI layers.

REFERENCES CITED

- [1] P. Verma, P. Maire, and P. Novák, "A review of the features and analyses of the solid electrolyte interphase in Li-ion batteries," *Electrochim. Acta*, vol. 55, no. 22, pp. 6332–6341, 2010.
- [2] D. Aurbach, "Review of selected electrode-solution interactions which determine the performance of Li and Li ion batteries," *J. Power Sources*, vol. 89, no. 2, pp. 206–218, 2000.
- [3] Q. Wang, J. Sun, X. Yao, and C. Chen, "Thermal Behavior of Lithiated Graphite with Electrolyte in Lithium-Ion Batteries," *J. Electrochem. Soc.*, vol. 153, no. 2, pp. 329–333, 2006.
- [4] J. B. Goodenough and Y. Kim, "Challenges for Rechargeable Li Batteries," *Chem. Mater.*, vol. 22, no. 3, pp. 587–603, 2010.
- [5] S. Phul, A. Deshpande, and B. Krishnamurthy, "A Mathematical model to study the effect of potential drop across the SEI layer on the capacity fading of a lithium ion battery," *Electrochim. Acta*, vol. 164, pp. 281–287, 2015.
- [6] M. B. Pinson and M. Z. Bazant, "Theory of SEI Formation in Rechargeable Batteries: Capacity Fade, Accelerated Aging and Lifetime Prediction," *J. Electrochem. Soc.*, vol. 160, no. 2, pp. A243–A250, 2013.
- [7] H. Yang and X. D. Shen, "Dynamic TGA-FTIR studies on the thermal stability of lithium/graphite with electrolyte in lithium-ion cell," *J. Power Sources*, vol. 167, no. 2, pp. 515–519, 2007.
- [8] N. Choi, I. A. Profatilova, S. Kim, and E. Song, "Thermochimica Acta Thermal reactions of lithiated graphite anode in LiPF₆-based electrolyte," *Thermochim. Acta*, vol. 480, no. 1–2, pp. 10–14, 2008.
- [9] S. S. Zhang, "A review on electrolyte additives for lithium-ion batteries," *J. Power Sources*, vol. 162, no. 2 SPEC. ISS., pp. 1379–1394, 2006.
- [10] K. Xu, S. S. Zhang, U. Lee, J. L. Allen, and T. R. Jow, "LiBOB: Is it an alternative salt for lithium ion chemistry?," *J. Power Sources*, vol. 146, no. 1–2, pp. 79–85, 2005.
- [11] L. E. Downie, K. J. Nelson, R. Petibon, V. L. Chevrier, and J. R. Dahn, "The Impact of Electrolyte Additives Determined Using Isothermal Microcalorimetry," *ECS Electrochem. Lett.*, vol. 2, no. 10, pp. 106–109, 2013.
- [12] H. Ota, Y. Sakata, A. Inoue, and S. Yamaguchi, "Analysis of Vinylene Carbonate Derived SEI Layers on Graphite Anode," *J. Electrochem. Soc.*, vol. 151, no. 10, p. A1659, 2004.

- [13] Z. Li, J. Huang, B. Yann Liaw, V. Metzler, and J. Zhang, "A review of lithium deposition in lithium-ion and lithium metal secondary batteries," *J. Power Sources*, vol. 254, pp. 168–182, 2014.
- [14] C. M. Julien, A. Mauger, K. Zaghib, and H. Groult, "Comparative Issues of Cathode Materials for Li-Ion Batteries," *Inorganics*, vol. 2, pp. 132–154, 2014.
- [15] D. Aurbach, E. Zinigrad, Y. Cohen, and H. Teller, "A short review of failure mechanisms of lithium metal and lithiated graphite anodes in liquid electrolyte solutions," *Solid State Ionics*, vol. 148, no. 3–4, pp. 405–416, 2002.
- [16] R. Teki, R. Krishnan, T. C. Parker, T. M. Lu, P. N. Kumta, and N. Koratkar, "Nanostructured silicon anodes for lithium Ion rechargeable batteries," *Small*, vol. 5, no. 20, pp. 2236–2242, 2009.
- [17] V. Aravindan, J. Gnanaraj, S. Madhavi, and H. K. Liu, "Lithium-ion conducting electrolyte salts for lithium batteries," *Chem. - A Eur. J.*, vol. 17, no. 51, pp. 14326–14346, 2011.
- [18] Z. Chen, W. Q. Lu, J. Liu, and K. Amine, "LiPF₆/LiBOB blend salt electrolyte for high-power lithium-ion batteries," *Electrochim. Acta*, vol. 51, no. 16, pp. 3322–3326, 2006.
- [19] R. Marom, O. Haik, D. Aurbach, and I. C. Halalay, "Revisiting LiClO₄ as an Electrolyte for Rechargeable Lithium-Ion Batteries," *J. Electrochem. Soc.*, vol. 157, no. 8, p. A972, 2010.
- [20] L. Larush-Asraf, M. Biton, H. Teller, E. Zinigrad, and D. Aurbach, "On the electrochemical and thermal behavior of lithium bis(oxalato)borate (LiBOB) solutions," *J. Power Sources*, vol. 174, no. 2, pp. 400–407, 2007.
- [21] M. Nie and B. L. Lucht, "Role of Lithium Salt on Solid Electrolyte Interface (SEI) Formation and Structure in Lithium Ion Batteries," *J. Electrochem. Soc.*, vol. 161, no. 6, pp. A1001–A1006, 2014.
- [22] K. Edström, M. Herstedt, and D. P. Abraham, "A new look at the solid electrolyte interphase on graphite anodes in Li-ion batteries," *J. Power Sources*, vol. 153, no. 2, pp. 380–384, 2006.
- [23] P. Arora, R. E. White, and M. Doyle, "Capacity Fade Mechanisms and Side Reactions in Lithium-Ion Batteries," *J. Electrochem. Soc.*, vol. 145, no. 10, pp. 3647–3667, 1998.
- [24] T. Yoshida, M. Takahashi, S. Morikawa, C. Ihara, H. Katsukawa, T. Shiratsuchi, and J. Yamaki, "Degradation Mechanism and Life Prediction of Lithium-Ion Batteries," *J. Electrochem. Soc.*, vol. 153, no. 3, p. A576, 2006.
- [25] J. G. Thevenin and R. H. Muller, "Impedance of Lithium Electrodes in a Propylene Carbonate Electrolyte," *J. Electrochem. Soc.*, vol. 134, no. 2, pp. 273–280, 1987.

- [26] R. Jorn, R. Kumar, D. P. Abraham, and G. A. Voth, “Atomistic Modeling of the Electrode – Electrolyte Interface in Li-Ion Energy Storage Systems : Electrolyte Structuring,” 2013.
- [27] S. Kim, A. C. T. Van Duin, and V. B. Shenoy, “Effect of electrolytes on the structure and evolution of the solid electrolyte interphase (SEI) in Li-ion batteries : A molecular dynamics study,” *J. Power Sources*, vol. 196, no. 20, pp. 8590–8597, 2011.
- [28] P. Lu and S. J. Harris, “Lithium transport within the solid electrolyte interphase,” *Electrochem. commun.*, vol. 13, no. 10, pp. 1035–1037, 2011.
- [29] Z. Yang, M. C. Dixon, R. A. Erck, and L. Trahey, “Quantification of the Mass and Viscoelasticity of Interfacial Films on Tin Anodes Using EQCM-D,” *ACS Appl. Mater. Interfaces*, vol. 7, no. 48, pp. 26585–26594, 2015.
- [30] S. Shi, P. Lu, Z. Liu, Y. Qi, L. G. Hector, H. Li, and S. J. Harris, “Direct calculation of Li-ion transport in the solid electrolyte interphase,” *J. Am. Chem. Soc.*, vol. 134, no. 37, pp. 15476–15487, 2012.
- [31] H. Zheng, Jieyun;Zheng, Hao;Wang, Rui;Ben, Liubin;Lu, Wei;Chen, Liwei;Chen, Liquan;Li, “3D visualization of inhomogeneous multi-layered structure and Young’s modulus of the solid electrolyte interphase (SEI) on silicon anodes for lithium ion batteries,” *Phys. Chem. Chem. Phys.*, vol. 16, no. 26, pp. 13229–13238, 2014.
- [32] D. Aurbach, M. Moshkovich, Y. Cohen, and A. Schechter, “The Study of Surface Film Formation on Noble-Metal Electrodes in Alkyl Carbonates / Li Salt Solutions , Using Simultaneous in Situ AFM , EQCM , FTIR , and EIS,” *Langmuir*, vol. 15, no. 9, pp. 2947–2960, 1999.
- [33] M. Moshkovich, Y. Gofer, and D. Aurbach, “Investigation of the Electrochemical Windows of Aprotic Alkali Metal (Li, Na, K) Salt Solutions,” *J. Electrochem. Soc.*, vol. 148, no. 4, pp. E155–E167, 2001.
- [34] S. H. Kang, D. P. Abraham, A. Xiao, and B. L. Lucht, “Investigating the solid electrolyte interphase using binder-free graphite electrodes,” *J. Power Sources*, vol. 175, no. 1, pp. 526–532, 2008.
- [35] H. Yildirim, A. Kinaci, M. K. Y. Chan, and J. P. Greeley, “First-Principles Analysis of Defect Thermodynamics and Ion Transport in Inorganic SEI Compounds: LiF and NaF,” *ACS Appl. Mater. Interfaces*, vol. 7, no. 34, pp. 18985–18996, 2015.
- [36] G. V. Zhuang, G. Chen, J. Shim, X. Song, P. N. Ross, and T. J. Richardson, “Li₂CO₃ in LiNi_{0.8}Co_{0.15}Al_{0.05}O₂ cathodes and its effects on capacity and power,” *J. Power Sources*, vol. 134, no. 2, pp. 293–297, 2004.
- [37] D. Aurbach, E.-E. Yair, O. Chusid, Y. Carmeli, M. Babai, and H. Yamin, “The Correlation Between the Surface Chemistry and the Performance of Li-Carbon Intercalation Anodes for Rechargeable ‘Rocking-Chair’ Type Batteries,” *J. Electrochem. Soc.*, vol. 141, no. 3, pp. 603–611, 1994.

- [38] N. Katayama, T. Kawamura, Y. Baba, and J. Yamaki, "Thermal stability of propylene carbonate and ethylene carbonate \pm propylene carbonate-based electrolytes for use in Li cells," *J. Power Sources*, vol. 109, no. 2, pp. 321–326, 2002.
- [39] I. A. Profatilova, S. Kim, and N. Choi, "Electrochimica Acta Enhanced thermal properties of the solid electrolyte interphase formed on graphite in an electrolyte with fluoroethylene carbonate," *Electrochim. Acta*, vol. 54, no. 19, pp. 4445–4450, 2009.
- [40] M. Inaba, H. Tomiyasu, A. Tasaka, S.-K. Jeong, and Z. Ogumi, "Atomic force microscopy study on the stability of a surface film formed on a graphite negative electrode at elevated temperatures," *Langmuir*, vol. 20, no. 4, pp. 1348–55, 2004.
- [41] M. Ryou, J. Lee, D. Jin, W. Kim, Y. Kyeong, J. Wook, J. Park, and Y. Min, "Electrochimica Acta Effects of lithium salts on thermal stabilities of lithium alkyl carbonates in SEI layer," *Electrochim. Acta*, vol. 83, pp. 259–263, 2012.
- [42] S. Sloop, J. Pugh, S. Wang, J. Kerr, and KinoshitaK, "Chemical reactivity of PF5 and LiPF6 in ethylene carbonate/dimethyl carbonate solutions," *Electrochem. Solid State Lett.*, vol. 4, no. 4, p. A420A44, 2001.
- [43] M. Nie, D. P. Abraham, Y. Chen, A. Bose, and B. L. Lucht, "Silicon Solid Electrolyte Interphase (SEI) of Lithium Ion Battery Characterized by Microscopy and Spectroscopy Silicon solid electrolyte interphase (SEI) of lithium ion battery characterized by microscopy and spectroscopy," *J. Phys. Chem. C*, vol. 117, no. 26, pp. 13403–13412, 2013.
- [44] B. Meyer, N. Leifer, S. Sakamoto, S. Greenbaum, and C. Grey, "High field multinuclear NMR investigation of the SEI layer in lithium rechargeable batteries," *Electrochem. Solid State Lett.*, vol. 8, no. 3, pp. A145–A148, 2005.
- [45] J. E. Owejan, J. P. Owejan, S. C. Decaluwe, and J. A. Dura, "Solid Electrolyte Interphase in Li-Ion Batteries: Evolving Structures Measured In situ by Neutron Reflectometry," *Chem. Mater.*, vol. 24, no. 11, pp. 2133–2140, 2012.
- [46] J. F. Browning, K. L. Jungjohann, Y. Wang, W. E. Tenhae, J. K. Keum, D. L. Wood, and G. M. Veith, "In Situ Determination of the Liquid/Solid Interface Thickness and Composition for the Li Ion Cathode LiMn_{1.5}Ni_{0.5}O₄," *ACS Appl. Mater. Interfaces*, vol. 6, no. 21, pp. 18569–18576, 2014.
- [47] B. Jerliu, R. Steitz, V. Oberst, U. Geckle, M. Bruns, and H. Schmidt, "Volume Expansion during Lithiation of Amorphous Silicon Thin Film Electrodes Studied by In-Operando Neutron Reflectometry," *J. Phys. Chem. C*, vol. 118, no. 18, pp. 9395–9399, 2014.
- [48] G. M. Veith, M. Doucet, J. K. Baldwin, R. L. Sacci, T. M. Fears, Y. Wang, and J. F. Browning, "Direct Determination of Solid-Electrolyte Interphase Thickness and Composition as a Function of State of Charge on a Silicon Anode," *J. Phys. Chem. C*, vol. 119, no. 35, pp. 20339–20349, 2015.

- [49] T. M. Fears, M. Doucet, J. F. Browning, J. K. S. Baldwin, J. G. Winiarz, H. Kaiser, H. Taub, R. L. Sacci, and G. M. Veith, "Evaluating the solid electrolyte interphase formed on silicon electrodes : a comparison of ex situ X-ray photoelectron spectroscopy and in situ neutron reflectometry," *Phys. Chem. Chem. Phys.*, vol. 18, no. 20, pp. 13927–13940, 2016.
- [50] H. Kawaura, M. Harada, Y. Kondo, H. Kondo, Y. Suganuma, N. Takahashi, J. Sugiyama, Y. Seno, and N. L. Yamada, "Operando Measurement of Solid Electrolyte Interphase Formation at Working Electrode of Li-Ion Battery by Time-Slicing Neutron Reflectometry," *ACS Appl. Mater. Interfaces*, vol. 8, no. 15, pp. 9540–9544, 2016.
- [51] D. Aurbach and Y. Gofer, *Nonaqueous Electrochemistry*. New York: Marcel Dekker, 1999.
- [52] E. Peled and J. P. Gabano, *Lithium Batteries*. New York: Academic Press, 1983.
- [53] S. C. Decaluwe, P. A. Kienzle, P. Bhargava, M. Baker, and J. A. Dura, "Phase segregation of sulfonate groups in Nafion interface lamellae, quantified via neutron structures," *Soft Matter*, vol. 10, no. 31, pp. 5763–5776, 2014.
- [54] P. A. Kienzle, J. A. Krycka, and P. N., "Refl1D: Interactive Depth Profile Modeler." Available: <http://www.reflectometry.org/danse/software.html>.
- [55] "QCM-D Technology," *Biolin Scientific*, 2016. [Online]. Available: <http://www.biolinscientific.com/technology/qcm-d-technology/>.
- [56] B. K. M V Voinova and M Rodahl and M Jonson and B Kasemo, "Viscoelastic Acoustic Response of Layered Polymer Films at Fluid-Solid Interfaces: Continuum Mechanics Approach," *Phys. Scr.*, vol. 59, no. 5, p. 391, 1999.
- [57] E. Lassner and W.-D. Schubert, *Tungsten*. Springer US, 1999.
- [58] J. I. Watjen, T. J. Bright, Z. M. Zhang, C. Muratore, and A. A. Voevodin, "Spectral radiative properties of tungsten thin films in the infrared," *Int. J. Heat Mass Transf.*, vol. 61, pp. 106–113, 2013.
- [59] R. Zhang, Z. Huo, X. Jiao, H. Zhong, and Y. Shi, "Deposition of Tungsten Thin Films on Flexible Polymer Substrates by Direct-Current Magnetron Sputtering," *J. Electron. Mater.*, vol. 44, no. 11, pp. 4557–4562, 2015.
- [60] H. Kolb, D. M; Przasnyski, M.; Gerischer, "Underpotential Deposition of Metals and Work Function Differences," *Electroanal. Chem. Interfacial Electrochem.*, vol. 54, pp. 25–38, 1974.
- [61] D. Aurbach, "A Comparative Study of Synthetic Graphite and Li Electrodes in Electrolyte Solutions Based on Ethylene Carbonate-Dimethyl Carbonate Mixtures," *J. Electrochem. Soc.*, vol. 143, no. 12, p. 3809, 1996.

- [62] R. E. Kass, A. E. Raftery, "Bayes Factors," *J. Amer. Statistical Assoc.*, vol. 90, no. 430, p. 773-795, 1995.

APPENDIX A – NR FITTING PYTHON SCRIPTS

A.1 W1_bare and W1_ocv Simultaneous Fitting Script

```
from refl1d.names import *
from numpy import arange, linspace

Probe.view = 'log'

SiOx_SLD = 3.4688
SiOx_irho = 0.00000985
W_SLD = 2.998
W_irho = 0.003214
WOx_SLD = 4.1
WOx_irho = 0.001
elyte_SLD = 3.77

data_file_bare = '3bare_He.refl'
data_file_ocv = 'w3ocv_first.refl'

instrument = NCNR.ANDR(Tlo=0.5, slits_at_Tlo=0.2, slits_below=0.05)

probe_bare = instrument.load(data_file_bare)
probe_ocv = instrument.load(data_file_ocv)

### SLDs
rho_SiOxin = Parameter(name="SiOxinDensity", value=1.14489)
rho_SiOxout = Parameter(name="SiOxoutDensity", value=1.04357)
rho_W_bare = Parameter(name="TungstenDensity_Bare", value=0.9787)
rho_WOx_bare = Parameter(name="WOxDensity_Bare", value=1.0)
rho_elyte = Parameter(name="elyteDensity", value=1.0)
W_elyte_filled_ratio = Parameter(name="W_Elyte_Filled_Ratio", value=0.5)

SiOx_in = SLD(name="SiOxin", rho=rho_SiOxin*SiOx_SLD, irho=rho_SiOxin*SiOx_irho)
SiOx_out = SLD(name="SiOxout", rho=rho_SiOxout*SiOx_SLD,
               irho=rho_SiOxout*SiOx_irho)

W_bare = SLD(name="W_bare", rho=rho_W_bare*W_SLD, irho=rho_W_bare*W_irho)
W_ocv = SLD(name="W_ocv", rho=rho_W_bare*W_SLD + W_elyte_filled_ratio*(1-
               rho_W_bare)*rho_elyte*elyte_SLD, irho=rho_W_bare*W_irho)

WOx_bare = SLD(name="WOx_bare", rho=rho_WOx_bare*WOx_SLD,
               rho=rho_WOx_bare*WOx_irho)
WOx_ocv = SLD(name="WOx_ocv", rho=1)

elyte = SLD(name="elyte", rho=rho_elyte*elyte_SLD)
```

```

sei = SLD(name="sei", rho=2)

### Interfaces
Si_SiOx = Parameter(name="Si:SiOx", value=0.0326474)
SiOxin_SiOxout = Parameter(name="SiOxin:SiOxout", value=0.0821796)

SiOx_W_bare = Parameter(name="SiOx:W_bare", value=12.9251)
SiOx_W_ocv = Parameter(name="SiOx:W_ocv", value=12.9251)

W_WOx_bare = Parameter(name="W:WOx_bare", value=0.273827)
W_WOx_ocv = Parameter(name="W:WOx_ocv", value=0.273827)

WOx_air = Parameter(name="WOx:air", value=0.3)
WOx_sei = Parameter(name="WOx:sei", value=0.3)
sei_elyte = Parameter(name="sei:elyte", value=100)

### Thicknesses
SiOxin_th = Parameter(name="SiOxin_thickness", value=23.0619)
SiOxout_th = Parameter(name="SiOxout_thickness", value=84.9364)

W_th_bare = Parameter(name="W_thickness_bare", value=149.5)
W_th_ocv = Parameter(name="W_thickness_ocv", value=149.5)

WOx_th_bare = Parameter(name="WOx_thickness_bare", value=19)
WOx_th_ocv = Parameter(name="WOx_thickness_ocv", value=19)

sei_th = Parameter(name="sei_thickness", value=100)

### Samples
sample_bare = silicon(0,Si_SiOx) | SiOx_in(SiOxin_th,SiOxin_SiOxout) |
    SiOx_out(SiOxout_th,SiOx_W_bare) | W_bare(W_th_bare,W_WOx_bare) |
    WOx_bare(WOx_th_bare,WOx_air) | air

sample_ocv = elyte(0,sei_elyte*sei_th) | sei(sei_th,WOx_sei*WOx_th_ocv) |
    WOx_ocv(WOx_th_ocv,W_WOx_ocv*WOx_th_ocv) | W_ocv(W_th_ocv,SiOx_W_ocv)
    | SiOx_out(SiOxout_th,SiOxin_SiOxout) | SiOx_in(SiOxin_th,Si_SiOx) | silicon

### Fitting Parameters

#SLDs
rho_W_bare.range(0.85,1.0)
W_elyte_filled_ratio.range(-10,10)
rho_WOx_bare.range(0,1.0)
WOx_ocv.rho.range(0.1,3.0)
sei.rho.range(0,4)
rho_elyte.range(0.7,1.2)

```

```

#Thicknesses
W_th_bare.range(125,175)
W_th_ocv.range(125,175)
WOx_th_bare.range(0,100)
WOx_th_ocv.range(0,100)
sei_th.range(0,750)

#Interfaces
SiOx_W_bare.range(0,30)
SiOx_W_ocv.range(0,30)
W_WOx_bare.range(0,0.4)
W_WOx_ocv.range(0,0.4)
WOx_air.range(0,0.4)
WOx_sei.range(0,0.4)
sei_elyte.range(0,0.4)

#Experimental Parameters
theta_offset_bare = Parameter(name="Theta_offset_bare", value=0)
theta_offset_ocv = Parameter(name="Theta_offset_ocv", value=0)
intensity_bare = Parameter(name="Intensity_bare", value=1)
intensity_ocv = Parameter(name="Intensity_ocv", value=1)
background_bare = Parameter(name="Background_bare", value=1)
background_ocv = Parameter(name="Background_ocv", value=1)

probe_bare.theta_offset = theta_offset_bare
probe_bare.intensity = intensity_bare
probe_bare.background = background_bare*1e-6
probe_ocv.theta_offset = theta_offset_ocv
probe_ocv.intensity = intensity_ocv
probe_ocv.background = background_ocv*1e-6

theta_offset_bare.range(-0.005,0.005)
intensity_bare.range(0.7,1.2)
intensity_ocv.range(0.7,1.2)
background_bare.range(0,5)
background_ocv.range(0,5)

M_bare = Experiment(probe=probe_bare, sample=sample_bare)
M_ocv = Experiment(probe=probe_ocv, sample=sample_ocv)

problem = MultiFitProblem([M_bare, M_ocv])

```

A.2 W2_electrolyte Fitting Script

```
from refl1d.names import *
from numpy import arange, linspace

Probe.view = 'log'

SiOx_SLD = 3.4688
SiOx_irho = 0.00000985
W_SLD = 2.998
W_irho = 0.003214
WOx_SLD = 4.1
WOx_irho = 0.001
elyte_SLD = 3.77
elyte_irho = 0.001

data_file = 'w4elt.refl'

instrument = NCNR.ANDR(Tlo=0.5, slits_at_Tlo=0.2, slits_below=0.05)
probe = instrument.load(data_file)

rho_SiOxin = Parameter(name="SiOxinDensity", value=1.14489)
rho_SiOxout = Parameter(name="SiOxoutDensity", value=1.04357)
rho_W = Parameter(name="TungstenDensity", value=1.0)
rho_WOx = Parameter(name="WOxDensity", value=1.0)
rho_elyte = Parameter(name="elyteDensity", value=1.0)

W_WOx = Parameter(name="W:WOx", value=0.3)
Surf_elyte = Parameter(name="WOx:elyte", value=0.5)

SiOx_in = SLD(name="SiOxout", rho=3.9714, irho=1.02795e-5)
SiOx_out = SLD(name="SiOxin", rho=3.61994, irho=1.1277e-5)
W = SLD(name="W", rho=W_SLD, irho=W_irho)
WOx = SLD(name="WOx", rho=WOx_SLD, irho=WOx_irho)
elyte = SLD(name="elyte", rho=elyte_SLD, irho=elyte_irho)

###Samples
sample = elyte(0, Surf_elyte) | WOx(19.2498, W_WOx) | W(139.2, 5.6198) |
    SiOx_out(84.9364, 0.08218) | SiOx_in(23.062, 0.03265) | silicon

###Fitting Parameters
sample[4].material.rho.pmp(10)
sample[4].thickness.pmp(20)

sample[3].material.rho.pmp(10)
```

```

sample[3].thickness.pmp(20)

sample[2].thickness.range(100,200)
rho_W.range(0.75,1.25)
sample[2].material.rho = rho_W*W_SLD
sample[2].material.irho = rho_W*W_irho

sample[1].thickness.range(50,400)
W_WOx.range(0,0.5)
sample[1].interface = W_WOx*sample[1].thickness
rho_WOx.range(0.25,2.5)
sample[1].material.rho = rho_WOx*WOx_SLD
sample[1].material.irho = rho_WOx*WOx_irho

rho_elyte.range(0.8,2.0)
Surf_elyte.range(0,4)
sample[0].interface = Surf_elyte*sample[1].thickness
sample[0].material.rho = rho_elyte*elyte_SLD
sample[0].material.irho = rho_elyte*elyte_irho

theta_offset = Parameter(name='Theta_Offset',value=0)
theta_offset.range(-0.005,0.005)
probe.theta_offset = theta_offset

intensity = Parameter(name='Intensity',value=1.0)
intensity.range(0.7,1.2)
probe.intensity = intensity

BK = Parameter(name="Background", value=0.3)
BK.range(0,10)
probe.background = BK*1e-6

M = Experiment(probe=probe, sample=sample)
problem = FitProblem(M)

```